MASTER

Mutual coupling between a wire antenna of finite conductivity and a large object

Vossen, S.H.J.A.

Award date:
1997

TECHNISCHE UNIVERSITEIT EINDHOVEN

FACULTEIT ELEKTROTECHNIEK

VAKGROEP TTE

LEERSTOELGEBIED Elektromagnetisme

Mutual coupling between a wire antenna of finite conductivity and a large object

door

S.H.J.A. Vossen

EM-7-97

Verslag van een afstudeeronderzoek,
verricht in de vakgroep TTE,
onder begeleiding van
dr.ir. A.P.M. Zwamborn (TNO-FEL) en
prof.dr. A.G. Tijhuis,
in de periode van mei 1996 - april 1997.

Eindhoven, juni 1997

Abstract

To obtain better insight into the electromagnetic interaction between an antenna and a dielectric body, for instance the human head, the full three-dimensional electromagnetic-wave equation is solved numerically. First, we derive a general representation for the magnetic and electric field quantities. This is done for both electrically impenetrable objects and lossy dielectric objects. A general form to represent the mutual coupling between two objects follows in a straightforward manner. The coupling equations obtained are solved by using the Weak Conjugate-Gradient Fast Fourier-Transformation method. As a pilot study, we consider the mutual coupling between two wire antennas. In this problem we have one active wire antenna, which is driven with a delta-gap voltage source and one passive wire antenna. In our model of the two mutually coupled wire antennas, we account for finite conductivity by an approximation which is demonstrated to be accurate. Finally, results are presented for the antenna-body problem in its simplest form, namely for a radially layered sphere and a dipole antenna. The extension of this model to more complex dielectric structures is a topic for future research.

Contents

Chapter 1

Introduction

During the past several years, there has been an increasing interest in the possible hazards of electromagnetic radiation to our health. Especially the extensive growth in the use of cellular phones has caused all kinds of speculations about possible hazards. The reported effects vary from getting cancer to becoming more nervous than usual. This problem drew, and continues to draw, the attention of many researchers throughout the world. The interest in the effects of electromagnetic radiation was initiated by the use of radar. In the early 1950's several researchers investigated the possible effects on humans of non-lethal radar systems. In the late 1950's researchers became aware that not only radar, but also other electromagnetic radiation sources could be hazardous to our health. A few years later, computers became powerful enough to simulate the behavior of simple models of man exposed to a plane wave. In the early 1970's, researchers started to simulate the effects of a plane wave that illuminates a dielectric body.

The general method for describing a model of man was the integral-equation method. This method has been used extensively in computing the effects of electromagnetic waves on models of man.
Since the late 1980's, a lot of researchers switched to the finite-difference time-domain (FDTD) method, because this method is far more easy to implement on a computer system, and therefore the formulation of the problem becomes a lot easier. This does not mean that researchers forgot about the integral-equation methods, but these methods became a less important tool in computing these kinds of problems. Another reason for the intensified use of FDTD methods is the fact that coupling problems are difficult to implement on a computer when written in integral-equation form. However the FDTD method has some major disadvantages. These disadvantages are:

- Special care has to be taken in order to correctly implement a wire antenna and other structures that involve surface currents.
- Excessive use of memory due to the storage of the space surrounding the objects under study, especially if the antenna is at some distance of the dielectric object.

In this report, we will describe the coupling between a wire antenna and a three-dimensional object with the aid of integral equations. Originally, the wire antenna was chosen to be perfectly conducting. During the research to model this coupling problem, we also derived an integral equation for a wire antenna with a finite conductivity. This allows us to model the antennas with realistic material parameters.

In the next chapter, we will give an historical overview of the research that has been carried out into the effects of electromagnetic radiation on realistic models of man in the past 25 years. In Chapter 3, we derive the general form of the integral equations for scattering by both a perfectly conducting object and a dielectric object. The equations will be derived for a three-dimensional problem, since the equations for a two- or one-dimensional problem can be found as simplifications of the three-dimensional form. Some basic mathematical tools are presented, which are needed for deriving the integral equations involved. The general form to describe the coupling between two objects is derived as well. In Chapter 4, we present two forms of the integral equations for describing the scattered electric field of a wire antenna. The first one is based on a classical approach by Pocklington [24] and the second one is an approach that can handle wires with finite conductivity as well. The coupling between two wires will also be considered here, with one of the wires being excited by a delta-gap source. In Chapter 5, we derive the integral equations that describe the coupling problem between a wire antenna and a dielectric body. In this chapter we consider delta-gap excitation of the wire antenna. To arrive at the coupled integral equations, we first derive an integral representation for the scattered electric field of a biological body. The numerical implementation of the various integral equations is dealt with in Chapter 6. For simplicity, we only describe the numerical procedure for the two-wire problem here. Although the full three-dimensional antenna-body problem is not as easy as this one, we believe that this description provides a good insight in the weak conjugate-gradient FFT method (WCG-FFT). Chapter 6 also gives a brief description of weakening a function as it is used in the WCG-FFT method. Results for the various configurations that we tested with the numerical representations of the integral equations from Chapter 4 and 5 can be found in Chapter 7. Finally, we draw some conclusions and give a few recommendations for future research in Chapter 8.

Chapter 2

Coupling of electromagnetic waves to human tissue

Since the early 1950's, there has been an interest in the possible hazards of electromagnetic radiation. The complex geometries of biological objects, the need to model complex radiation fields from sources of practical interest and the various complex electromagnetic properties of the tissues involved made the application of numerical techniques almost essential in investigating the electromagnetic interactions with biological models of realistic geometries. Simple geometries, plane-wave illumination and the utilization of homogenous models significantly simplify the analysis. Such simplified models provide a good insight in the first-order effects of electromagnetic interactions with biological tissue.

Until 1974 the general opinion among researchers that a biological body could be modeled by using a homogeneous model of simple geometry received a wide support. The first investigations of a realistic model of men to this issue have been performed by Livesay and Chen in the early 1970's [21]. The authors investigated the influence of plane-wave illumination on a human body model of greater complexity than had been previously considered. They discovered that the simple models which had been used until then were inaccurate. Based on this research several other authors have performed similar studies [12], [16], [27] of this model.

A value that researchers were (and still are) particularly interested in is the specific absorption rate (SAR). This SAR specifies how much power is absorbed per unit of mass. All of these studies were conducted for frequencies between 20 MHz and 500 MHz. Some authors considered frequencies up to 1 GHz. The reason to use plane-wave illumination is that people are usually far enough away from the radiating source to allow the use of the far-field approximation for describing the incident field.

Later, it became clear that the effect of the mutual coupling between the electromagnetic source and the human body could perhaps not be neglected. The first ones to study this problem were Nyquist *et al.* [22], back in 1977. These authors studied the mutual coupling between a thin-wire antenna and a relatively simple biological body. This model was used again by Karimullah [17] [18] to study a more complex model of the human body.

All this research had one element in common, integral equations were used to describe the biological body and, when appropriate, the thin-wire antenna.

A second similarity that occurred in these methods of solution was that they all made use of the principal value of the integrals involved, which means that the integral is evaluated throughout the volume with the exception of a small volume at the point where the integral is singular. A good description of this principal value (PV) can be found in van Bladel [4].

Finally they all used the method of moments (MoM) to evaluate the discretized integral equations. During the years, several other computational techniques have been used to study the problem of biological tissue which is exposed to electromagnetic waves. Some of these commonly known techniques are: finite-element methods, finite volume methods, EFIT, conjugate-gradient (CG) algorithms and, last but not least, finite difference time domain (FDTD) methods. Especially this last method is widely used these days. The reason for this lies in the fact that it is rather easy to use compared to the other available techniques. Other fields of interest were (are) more realistic models of a human body (the use of tetrahedral cells instead of cubical cells in the discretized model), improving the computational method by analytical techniques, etc.

In the early 1980's cancer and possible cancer treatment became a hot issue in society. All kinds of possible treatments were studied by researchers all over the world. In addition to illumination of tumors with radioactive rays, studies were performed into the possibilities of using electromagnetic waves to "burn" the tumor [1], [14]. For an accurate simulation, a far more complex model of the human body is needed than what was used previously. Today, the use of electromagnetic waves in cancer treatment is still a not yet a generally accepted technique.

During the past several years the use of cellular phones took an explosive growth. As a consequence of this growth, the question whether the electromagnetic waves radiated by the antenna are hazardous to our health became of increasing importance. Researchers all over the world started to investigate the possible effects of electromagnetic waves on the human body. But still the answer has not been given. Of course the studies from the early 1970's using plane-wave illumination cannot be used, since, for instance, the human head is in the near field of the radiating antenna. To provide more insight in the electromagnetic heating of human tissue by an antenna of some portable transmitter, we investigate the mutual coupling of a thin-wire antenna and a model of the human head. The method of solution is a special form of the CG-method, which was first proposed by Zwamborn [34]. This method has proven to work excellently with a model of a biological body and plane-wave or point-source illumination.

But first we want to explain the method of moments in more detail, because it has been widely used and because it is the basis of the conjugate-gradient method. The FDTD methods are not further explained here. The reader is referred to the huge amount of literature (for example [20], [29]) that is available because of their wide use at the moment.

2.1 Method of moments

One of the most commonly known procedures to solve integral equations is the method of moments (MoM). This numerical procedure starts by dividing the object into small mathematical cells. If the cells are small enough, the electric field inside this cell may be assumed to have a simple local behavior. An integral equation is usually of the form

$$\int_{x' \in V} G(x - x')\mathbf{J}(x')dx' = \mathbf{E}(x), \tag{2.1}$$

where V represents the volume of the biological body. The other terms in the equation will be explained further on in this report. This equation can be written in operator notation as

$$LJ = E. \tag{2.2}$$

The problem usually is to find the response J when the linear operator L and the excitation E are known. The MoM starts with the selection of a finite set of expansion functions ϕ_i, $i = 1, ..., N$, which are used to construct an approximation of J

$$J \approx \sum_{i=1}^{N} J_i \phi_i(x'), \ x' \in V. \tag{2.3}$$

In this latter equation the coefficients J_i are unknowns to be determined. The substitution of the latter equation in Eq. (2.2) gives

$$\sum_{i=1}^{N} J_i L\phi_i(x) \approx E(x), \ x \in V. \tag{2.4}$$

This last equation is an approximation of (2.2) and has to be fully discretized in order to solve it on a computer. To do this we take the inner product of both terms in Eq. (2.4) with a set of testing functions W_j, $j = 1, ..., N$. This yields

$$\sum_{i=1}^{N} J_i \left\langle L\phi_i, W_j \right\rangle = \left\langle E, W_j \right\rangle, \ j = 1, ..., N, \tag{2.5}$$

which is usually written in the form

$$[Z][J] = [V], \tag{2.6}$$

where

$$[Z]_{ij} = \left\langle L\phi_i, W_j \right\rangle, \tag{2.7}$$

$$[I]_i = J_i, \tag{2.8}$$

$$[V]_j = \left\langle E, W_j \right\rangle. \tag{2.9}$$

The approximate solution is then obtained by calculating the coefficients J_i.
Another approach for solving this equation can be devised by forming the residual error

$$r_N = E - \sum_{i=1}^{N} \alpha_i L\phi_i. \tag{2.10}$$

Next, the constraint that the inner product of the residual error with each of the testing functions should be zero,‘ is enforced

$$\langle r_N, W_j \rangle = 0. \tag{2.11}$$

Substitution of the definition of the residual error in this latter equation then gives the same system of linear equations.

Chapter 3

Formulation of the problem

In this chapter, we will develop a method of solution for a general electromagnetic coupling problem for two objects denoted by A and B. In subsequent chapters, this general method will be rewritten to suit the two-wire problem. Finally, the antenna-body problem will be studied.

3.1 The general problem

In this section we look at a configuration as displayed in the figure below (see Figure 3.1). In this figure, we distinguish two bounded, three-dimensional subdomains $\mathcal{D}_A$ and $\mathcal{D}_B$ representing the interior of the objects under consideration. The boundaries of the objects A and B are the closed surfaces $\partial\mathcal{D}_A$ and $\partial\mathcal{D}_B$, respectively, which are both assumed to be sufficiently regular. The unbounded space exterior to the boundaries $\partial\mathcal{D}_A$ and $\partial\mathcal{D}_B$ of the objects is denoted by $\mathcal{D}_\infty$, which is homogeneous and lossless with constant permittivity $\epsilon(\mathbf{r}) = \epsilon_\infty$ and constant permeability $\mu(\mathbf{r}) = \mu_\infty$. The normals $\mathbf{n}_A$ and $\mathbf{n}_B$ on the surfaces of the objects point into $\mathcal{D}_\infty$ and are assumed to be piecewise continuous across $\partial\mathcal{D}_A$ and $\partial\mathcal{D}_B$, respectively.

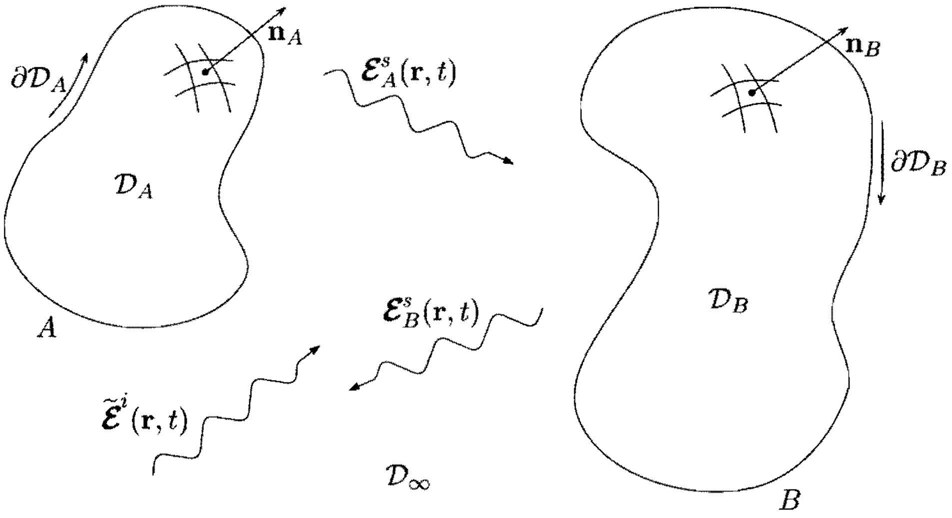

Figure 3.1: *A view of the general problem.*

We observe that both objects are illuminated and generate a scattered field. The scattered field of object A acts as a part of the total incident field on object B and vice versa. This effect is denoted as coupling. Consequently, the total incident field incident on one object consists of the scattered field radiated from the other object and $\tilde{\boldsymbol{\mathcal{E}}}^i(\mathbf{r},t)$, the field that would be present in absence of both objects. This coupling increases the complexity of the electromagnetic field calculations inside or outside the objects.

We formulate this problem in terms of two coupled integral equations. To arrive at the relevant equations we proceed in three steps.

- First, we derive an integral representation for the field in a homogeneous, finite domain. The integral representation expresses the field anywhere inside the domain in terms of the impressed electric and magnetic current densities inside the domain and the tangential field components on the boundary.
- Second, the integral representations thus obtained are used to derive integral equations for the scattering by a single object. We consider two cases. For inhomogeneous, penetrable objects, the domain of the integral equation is the interior of the object. For perfectly conducting objects, the domain is the boundary. Homogeneous, penetrable objects, for which both types of formulations are available, are not addressed.
- Third, the integral equations for a single object are coupled with the equations for a second object.

3.2 Basic relations

3.2.1 Formulation of the problem

In this section an integral representation is derived for the field in a homogeneous, finite domain. First we look at Figure 3.2. The domain $\mathcal{D}$ is bounded by $\partial\mathcal{D}$. The unbounded space exterior to $\partial\mathcal{D}$ is denoted as $\overline{\mathcal{D}}$ and is homogeneous and lossless with constant permittivity $\epsilon(\mathbf{r}) = \epsilon$ and permeability $\mu(\mathbf{r}) = \mu$. The normal $\mathbf{n}$ on the surface of $\mathcal{D}$ points into $\overline{\mathcal{D}}$ and is assumed to be piecewise continuous across $\partial\mathcal{D}$. We assume an electric current density $\boldsymbol{\mathcal{J}}^e(\mathbf{r},t)$ and a magnetic current density $\boldsymbol{\mathcal{J}}^m(\mathbf{r},t)$ to be present in the homogeneous, lossless medium $\overline{\mathcal{D}}$. The entire space will be denoted by $\mathbb{R}^3$.

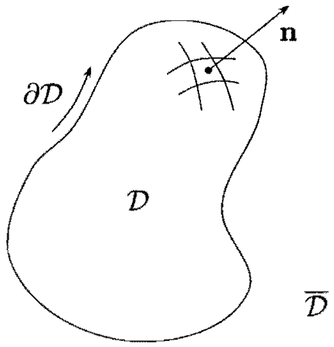

Figure 3.2: *Interior and exterior domain for derivation of the integral relations.*

Maxwell's equations in the time domain

The electromagnetic behavior of the object can be described with the aid of Maxwell's equations in the time domain

$$\nabla \times \boldsymbol{\mathcal{E}}(\mathbf{r},t) + \mu(\mathbf{r})\partial_t \boldsymbol{\mathcal{H}}(\mathbf{r},t) = -\boldsymbol{\mathcal{J}}^m(\mathbf{r},t), \tag{3.1}$$

$$\nabla \times \boldsymbol{\mathcal{H}}(\mathbf{r},t) - \left[\epsilon(\mathbf{r})\partial_t + \sigma(\mathbf{r})\right] \boldsymbol{\mathcal{E}}(\mathbf{r},t) = \boldsymbol{\mathcal{J}}^e(\mathbf{r},t), \tag{3.2}$$

where we have introduced

$\boldsymbol{\mathcal{E}}(\mathbf{r},t)$ = electric-field strength [Vm^{-1}],

$\boldsymbol{\mathcal{H}}(\mathbf{r},t)$ = magnetic-field strength [Am^{-1}],

$\mu(\mathbf{r}) = \mu_0\mu_r(\mathbf{r})$ = permeability [Hm^{-1}],

μ_0 = permeability of vacuum [Hm^{-1}],

$\epsilon(\mathbf{r}) = \epsilon_0\epsilon_r(\mathbf{r})$ = permittivity [Fm^{-1}],

ϵ_0 = permittivity of vacuum [Fm^{-1}],

$\sigma(\mathbf{r})$ = conductivity [Ω^{-1}m^{-1}],

$\boldsymbol{\mathcal{J}}^e(\mathbf{r},t)$ = external electric current density [Am^{-2}],

$\boldsymbol{\mathcal{J}}^m(\mathbf{r},t)$ = external magnetic current density [Vm^{-2}].

Since we are dealing with electromagnetic fields in linear and time-invariant media, we take advantage of this fact by carrying out a Laplace transformation with respect to time. In the Laplace-transform domain (the so called s-domain), the time coordinate is eliminated and an electromagnetic field problem in space remains. Before we transform Maxwell's equations to the Laplace-transform domain, we discuss two integral transformations.

3.2.2 Integral transformations

Time-Laplace-transform domain analysis

Let us assume that the source is switched on at the instant $t = t_0$. Our interval of interest then is $t_0 \le t < \infty$. We may now define the so-called temporal Laplace transform as

$$\mathbf{F}(\mathbf{r},s) = \int_{t_0}^{\infty} \exp(-st)\boldsymbol{\mathcal{F}}(\mathbf{r},t)\,dt. \tag{3.3}$$

The integral on the right-hand side of Eq. (3.3) exists if the complex Laplace-transform parameter s satisfies $\mathrm{Re}(s) \ge 0$ and $\boldsymbol{\mathcal{F}}(\mathbf{r},t)$ is an integrable function with respect to time. In that case, $\mathbf{F}(\mathbf{r},s)$ is a single-valued analytic function of s in the half plane $\mathrm{Re}(s) \ge 0$. Symbolically, Eq. (3.3) is written as

$$\mathcal{L}\left\{\boldsymbol{\mathcal{F}}(\mathbf{r},t)\right\} = \mathbf{F}(\mathbf{r},s), \tag{3.4}$$

where $\mathcal{L}$ denotes the Laplace-transformation operator. Assuming zero initial values at $t = t_0$ then, according to Eq. (3.3), we obtain for the time derivative ∂_t of a function $\boldsymbol{\mathcal{F}}(\mathbf{r},t)$ the property

$$\mathcal{L}\left\{\partial_t\boldsymbol{\mathcal{F}}(\mathbf{r},t)\right\} = s\mathbf{F}(\mathbf{r},s). \tag{3.5}$$

Another property of the Laplace transform that is used is known as the shift property

$$\mathcal{L}\left\{\boldsymbol{\mathcal{F}}(\mathbf{r}, t-\tau)\right\} = \exp(-s\tau)\mathbf{F}(\mathbf{r}, s). \tag{3.6}$$

The temporal Laplace transformation as given in Eq. (3.3) has an inverse counterpart, which is defined as

$$\mathcal{L}^{-1}\left\{\mathbf{F}(\mathbf{r}, s)\right\} = \frac{1}{2\pi i}\int_{\beta-i\infty}^{\beta+i\infty} \exp(st)\mathbf{F}(\mathbf{r}, s)\, ds = \boldsymbol{\mathcal{F}}(\mathbf{r}, t). \tag{3.7}$$

This inversion integral in the complex s-plane is often denoted as the Bromwich inversion integral. By taking $\beta = \mathrm{Re}(s) \geq 0$ and $\boldsymbol{\mathcal{F}}(\mathbf{r}, t)$ a causal integrable function, we ensure that the integrand decreases fast enough as $|\mathrm{Im}(s)| \to \infty$.

The spatial Fourier transform

We define the spatial Fourier transform $\hat{\mathbf{V}}(\mathbf{k}, s)$ of a vector field $\mathbf{V}(\mathbf{r}, s)$ over the domain $\mathcal{D}$ as

$$\hat{\mathbf{V}}(\mathbf{k}, s) = \int_{\mathbf{r}\in\mathcal{D}} \mathbf{V}(\mathbf{r}, s)\exp(-i\mathbf{k}\cdot\mathbf{r})\, d\mathbf{r}, \tag{3.8}$$

where $\mathbf{k} = k_x\mathbf{u}_x + k_y\mathbf{u}_y + k_z\mathbf{u}_z$. If the vector field $\mathbf{V}(\mathbf{r}, s)$ is extended by the value zero for $\mathbf{r} \in \overline{\mathcal{D}}$ by applying a shape function as visualized in Figure 3.3, Eq. (3.8) can also be taken for $\mathbf{r} \in \mathbb{R}^3$. With the aid of the shape function $\mathcal{S}(\mathbf{r})$, Eq. (3.8) can be written as

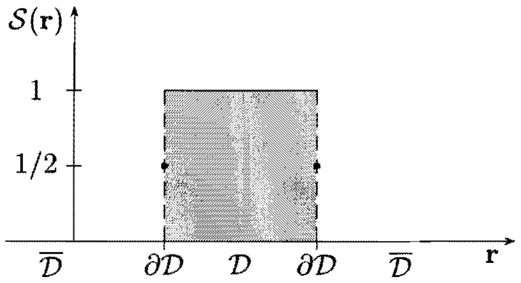

Figure 3.3: *The shape function* $\mathcal{S}(\mathbf{r})$.

$$\hat{\mathbf{V}}(\mathbf{k}, s) = \int_{\mathbf{r}\in\mathbb{R}^3} \mathbf{V}(\mathbf{r}, s)\mathcal{S}(\mathbf{r})\exp(-i\mathbf{k}\cdot\mathbf{r})\, d\mathbf{r}. \tag{3.9}$$

Symbolically Eq. (3.9) can be written as

$$\mathcal{F}\left\{\mathbf{V}(\mathbf{r}, s)\right\} = \hat{\mathbf{V}}(\mathbf{k}, s), \tag{3.10}$$

where $\mathcal{F}$ denotes the forward spatial Fourier transformation. Note the hat $\hat{}$ now represents a Fourier transformation of a spatially filtered function over the entire domain $\mathbb{R}^3$. In order to apply this transformation to Maxwell's equations in the Laplace domain, Eqs. (3.16) – (3.17), we need the corresponding transform of $\nabla\times\mathbf{V}(\mathbf{r}, s)$. By using Ostrogradsky's theorem

$$\int_{\mathbf{r}\in\mathcal{D}} \nabla\times\mathbf{V}(\mathbf{r})d\mathbf{r} = \oint_{\mathbf{r}\in\partial\mathcal{D}} \mathbf{n}(\mathbf{r})\times\mathbf{V}(\mathbf{r})d\mathbf{r}, \tag{3.11}$$

we find

$$\begin{aligned}\widehat{\nabla\times\mathbf{V}}(\mathbf{k},s) &= \int_{\mathbf{r}\in\mathcal{D}} \nabla\times[\mathbf{V}(\mathbf{r},s)\exp(-i\mathbf{k}\cdot\mathbf{r})]\,d\mathbf{r} - \int_{\mathbf{r}\in\mathcal{D}} [\nabla\exp(-i\mathbf{k}\cdot\mathbf{r})]\times\mathbf{V}(\mathbf{r},s)d\mathbf{r} \\ &= \oint_{\mathbf{r}\in\partial\mathcal{D}} [\mathbf{n}(\mathbf{r})\times\mathbf{V}(\mathbf{r},s)]\exp(-i\mathbf{k}\cdot\mathbf{r})d\mathbf{r} + i\mathbf{k}\times\int_{\mathbf{r}\in\mathcal{D}} \mathbf{V}(\mathbf{r},s)\exp(-i\mathbf{k}\cdot\mathbf{r})\,d\mathbf{r}. \quad (3.12)\end{aligned}$$

The forward spatial Fourier transformation as given in Eq. (3.9) also has an inverse counterpart, which we define as

$$\mathcal{S}(\mathbf{r})\mathbf{V}(\mathbf{r},s) = \left\{1,\frac{1}{2},0\right\}\mathbf{V}(\mathbf{r},s) = \frac{1}{8\pi^3}\int_{\mathbf{k}\in\mathbb{R}^3} \hat{\mathbf{V}}(\mathbf{k},s)\exp(i\mathbf{k}\cdot\mathbf{r})d\mathbf{k}, \qquad (3.13)$$

for $\mathbf{r}\in\{\mathcal{D},\ \partial\mathcal{D},\ \overline{\mathcal{D}}\}$. Symbolically Eq. (3.13) can be written as

$$\mathcal{F}^{-1}\left\{\hat{\mathbf{V}}(\mathbf{k},s)\right\} = \left\{1,\frac{1}{2},0\right\}\mathbf{V}(\mathbf{r},s), \qquad (3.14)$$

for $\mathbf{r}\in\{\mathcal{D},\ \partial\mathcal{D},\ \overline{\mathcal{D}}\}$. Further, the convolution of two functions $\hat{f}(\mathbf{r},s)$ and $\hat{g}(\mathbf{r},s)$ can be obtained by using the Fourier transformation as

$$\int_{\mathbf{r}'\in\mathbb{R}^3} f(\mathbf{r}-\mathbf{r}',s)g(\mathbf{r}')d\mathbf{r}' = \mathcal{F}^{-1}\left\{\hat{f}(\mathbf{k},s)\hat{g}(\mathbf{k},s)\right\}, \qquad (3.15)$$

which is known as the convolution theorem.

3.2.3 Maxwell's equations in the s-domain

Applying the Laplace transformation to the Maxwell equations in the time domain, Eqs. (3.1) – (3.2), we obtain Maxwell's equations in the s-domain

$$\nabla\times\mathbf{E}(\mathbf{r},s) + s\mu\mathbf{H}(\mathbf{r},s) = \mathbf{J}^m(\mathbf{r},s), \qquad (3.16)$$

$$\nabla\times\mathbf{H}(\mathbf{r},s) - [s\epsilon+\sigma]\,\mathbf{E}(\mathbf{r},s) = \mathbf{J}^e(\mathbf{r},s). \qquad (3.17)$$

Since the medium outside the object is homogenous and space-invariant, we take advantage of this by carrying out a Fourier transformation with respect to the spatial coordinates.

3.3 Source representations for the electromagnetic field in a finite, homogeneous domain

In this section we look at the configuration as depicted in Figure 3.4. We observe an impressed current density $\mathbf{J}_D(\mathbf{r},s)$ inside the domain $\mathcal{V}$. This current density can be of the magnetic type or of the electric type or of these two types together. The domain $\mathcal{V}$ is bounded by $\partial\mathcal{V}$. The normal $\mathbf{n}$ on the surface of $\mathcal{V}$ points into $\overline{\mathcal{V}}$ and is assumed to be piecewise continuous across $\partial\mathcal{V}$. Inside the domain $\mathcal{V}$, both permittivity and permeability are constant values.

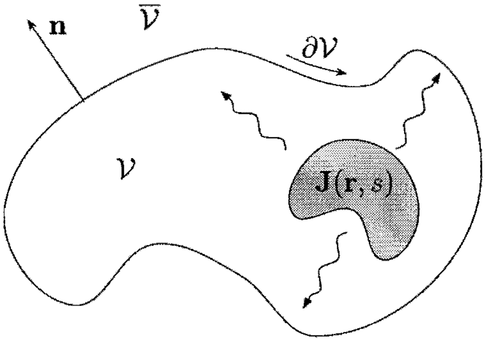

Figure 3.4: *Domain definitions for derivation of the integral representations.*

3.3.1 Solution in the transform domain

Subjecting Eqs. (3.16) – (3.17) to the spatial Fourier transformation over $\mathcal{V}$ yields

$$i\mathbf{k}\times\hat{\mathbf{H}}(\mathbf{k},s) - s\epsilon\hat{\mathbf{E}}(\mathbf{k},s) = \hat{\mathbf{J}}^e_D(\mathbf{k},s) + \hat{\mathbf{J}}^e_B(\mathbf{k},s), \tag{3.18}$$
$$i\mathbf{k}\times\hat{\mathbf{E}}(\mathbf{k},s) + s\mu\hat{\mathbf{H}}(\mathbf{k},s) = -\hat{\mathbf{J}}^m_D(\mathbf{k},s) - \hat{\mathbf{J}}^m_B(\mathbf{k},s), \tag{3.19}$$

in which $\hat{\mathbf{J}}^e_B(\mathbf{k},s)$ and $\hat{\mathbf{J}}^m_B(\mathbf{k},s)$ are the spatial transforms over the boundary $\partial\mathcal{V}$ of the quantities

$$\begin{aligned}\mathbf{J}^e_B(\mathbf{r},s) &= -\mathbf{n}(\mathbf{r})\times\mathbf{H}(\mathbf{r},s)\\ \mathbf{J}^m_B(\mathbf{r},s) &= \mathbf{n}(\mathbf{r})\times\mathbf{E}(\mathbf{r},s)\end{aligned}\ , \tag{3.20}$$

with $\mathbf{r}\in\partial\mathcal{V}$, and the subscripts $_D$ and $_B$ stand for "domain" and "boundary", respectively. Note that the conductivity $\sigma = 0$. In the spatial Fourier domain (**k**-domain) the spatial coordinates have been eliminated and algebraic equations remain. Note that in the right-hand sides of Eq. (3.20) the limiting values of the quantities upon approaching $\partial\mathcal{V}$ via $\mathcal{V}$ are to be taken. The structure of Eqs. (3.18) – (3.19) leads to the interpretation that $\mathbf{J}^e_B(\mathbf{r},s)$ and $\mathbf{J}^m_B(\mathbf{r},s)$ are the Laplace-transformed source densities of electric and magnetic surface currents.

We now have an algebraic system, that we can solve. As a result we obtain

$$\begin{aligned}\hat{\mathbf{H}}(\mathbf{k},s) = (k^2+\gamma^2)^{-1}\Big\{\ & i\mathbf{k}\times\left(\hat{\mathbf{J}}^e_D(\mathbf{k},s)+\hat{\mathbf{J}}^e_B(\mathbf{k},s)\right) - s\epsilon\left(\hat{\mathbf{J}}^m_D(\mathbf{k},s)+\hat{\mathbf{J}}^m_B(\mathbf{k},s)\right)\\ &+(s\mu)^{-1}i\mathbf{k}\left[i\mathbf{k}\cdot\left(\hat{\mathbf{J}}^m_D(\mathbf{k},s)+\hat{\mathbf{J}}^m_B(\mathbf{k},s)\right)\right]\Big\},\end{aligned} \tag{3.21}$$

and

$$\begin{aligned}\hat{\mathbf{E}}(\mathbf{k},s) = (k^2+\gamma^2)^{-1}\Big\{\ & -i\mathbf{k}\times\left(\hat{\mathbf{J}}^m_D(\mathbf{k},s)+\hat{\mathbf{J}}^m_B(\mathbf{k},s)\right) - s\mu\left(\hat{\mathbf{J}}^e_D(\mathbf{k},s)+\hat{\mathbf{J}}^e_B(\mathbf{k},s)\right)\\ &+(s\epsilon)^{-1}i\mathbf{k}\left[i\mathbf{k}\cdot\left(\hat{\mathbf{J}}^e_D(\mathbf{k},s)+\hat{\mathbf{J}}^e_B(\mathbf{k},s)\right)\right]\Big\},\end{aligned} \tag{3.22}$$

where $k = |\mathbf{k}| = (\mathbf{k}\cdot\mathbf{k})^{\frac{1}{2}}$ and $\gamma^2 = s^2\epsilon\mu$. At this point we would like to obtain an integral relation in the spatial domain by applying the inverse spatial Fourier transformation. To facilitate this, we first introduce Green's function.

3.3.2 Green's function in three dimensions

Green's function $\mathcal{G}(\mathbf{r},t)$ is defined as the causal solution of the three-dimensional Helmholz equation that is given by

$$(\nabla^2 - \frac{1}{c^2}\partial_t^2)\mathcal{G}(\mathbf{r},t) = -\delta(\mathbf{r})\delta(t), \tag{3.23}$$

in which c denotes the propagation velocity in the medium, equal to $(\epsilon\mu)^{-\frac{1}{2}}$, and $\delta(\mathbf{r})$ is the three-dimensional Dirac distribution. By subjecting Eq. (3.23) to a temporal Laplace and spatial Fourier transformation over $\mathbb{R}^3$, the following result is obtained

$$\hat{G}(\mathbf{k},s) = (k^2 + s^2/c^2)^{-1}. \tag{3.24}$$

The right-hand side of Eq. (3.24) is the same multiplicative factor that occurs in Eqs. (3.21) - (3.22). Therefore $\hat{\mathbf{H}}$ in Eq. (3.21) and $\hat{\mathbf{E}}$ in Eq. (3.22) can be regarded as a convolution with the Green's function in the spatial domain and the inverse Fourier- and Laplace transform of the remaining parts. In the three-dimensional space we transform $\hat{G}(\mathbf{k},s)$ to the spatial domain. The Green's function in the spatial domain is obtained by carrying out the inversion integral over the domain $\mathbb{R}^3$ as follows

$$\begin{aligned} G(\mathbf{r},s) &= \frac{1}{8\pi^3}\int_{\mathbf{k}\in\mathbb{R}^3} \hat{G}(\mathbf{k},s)\exp(i\mathbf{k}\cdot\mathbf{r})d\mathbf{k}, \\ &= \frac{1}{8\pi^3}\int_0^\infty dk \int_0^\pi d\theta_k \int_0^{2\pi} d\phi_k \frac{k^2\sin(\theta_k)}{k^2+s^2/c^2}\exp\left[ikr\cos(\theta_k)\right], \end{aligned} \tag{3.25}$$

where spherical coordinates have been introduced to represent the $\mathbf{k}$-domain and $r = |\mathbf{r}|$. Here, θ_k is the angle between $\mathbf{k}$ and $\mathbf{r}$ and ϕ_k the angle of rotation of $\mathbf{k}$ around $\mathbf{r}$. In Eq. (3.25), the integrals over ϕ_k and θ_k are elementary and we obtain

$$\begin{aligned} G(\mathbf{r},s) &= \frac{1}{4i\pi^2 r}\int_0^\infty \frac{k}{k^2+s^2/c^2}\left[\exp(-ikr) - \exp(ikr)\right]\, dk \\ &= \frac{1}{4i\pi^2 r}\int_{-\infty}^\infty \frac{\exp(-ikr)}{k^2+s^2/c^2}k\, dk. \end{aligned} \tag{3.26}$$

The integration with respect to k is performed by applying Cauchy's theorem and Jordan's lemma [5, pp. 71-75]. This leads to

$$G(\mathbf{r},s) = G(r,s) = \frac{\exp(-sr/c)}{4\pi r}. \tag{3.27}$$

3.3.3 Integral representation in the spatial domain

In this section we make use of the definition of Green's function and the integral representations Eq. (3.21) and Eq. (3.22) to formulate an integral representation in the spatial domain. Eqs. (3.21) - (3.22) can be rewritten as

$$\begin{aligned} \left\{1,\frac{1}{2},0\right\}\mathbf{H}(\mathbf{r},s) = \;& (s\mu)^{-1}\left(\nabla\nabla\cdot - \gamma^2\mathbf{I}\right)\left[\boldsymbol{A}_D^m(\mathbf{r},s) + \boldsymbol{A}_B^m(\mathbf{r},s)\right] \\ & +\nabla\times\left[\boldsymbol{A}_D^e(\mathbf{r},s) + \boldsymbol{A}_B^e(\mathbf{r},s)\right], \end{aligned} \tag{3.28}$$

and

$$\left\{1, \frac{1}{2}, 0\right\} \mathbf{E}(\mathbf{r}, s) = (s\epsilon)^{-1}\left(\nabla\nabla\cdot - \gamma^2\mathbf{I}\right)\left[\boldsymbol{A}_D^e(\mathbf{r}, s) + \boldsymbol{A}_B^e(\mathbf{r}, s)\right] - \nabla \times \left[\boldsymbol{A}_D^m(\mathbf{r}, s) + \boldsymbol{A}_B^m(\mathbf{r}, s)\right], \tag{3.29}$$

for $\mathbf{r} \in \left\{\mathcal{V}, \partial\mathcal{V}, \overline{\mathcal{V}}\right\}$. In Eq. (3.28) and Eq. (3.29) we have introduced the potentials

$$\boldsymbol{A}_D^{e,m}(\mathbf{r}, s) = \int_{\mathbf{r}' \in \mathcal{V}} G(\mathbf{r} - \mathbf{r}', s)\mathbf{J}_D^{e,m}(\mathbf{r}', s)d\mathbf{r}', \tag{3.30}$$

$$\boldsymbol{A}_B^{e,m}(\mathbf{r}, s) = \oint_{\mathbf{r}' \in \partial\mathcal{V}} G(\mathbf{r} - \mathbf{r}', s)\mathbf{J}_B^{e,m}(\mathbf{r}', s)d\mathbf{r}'. \tag{3.31}$$

In Eqs. (3.30) – (3.31), $\mathbf{r}$ is the point of observation and $\mathbf{r}'$ is a source point inside or on the surface of the object, respectively. By restricting the integration to these domains, we have accounted for the restrictions in the definitions of the Fourier transforms of these current densities.

With the integral relations Eq. (3.28) and Eq. (3.29), we now have at our disposal the basic relations to obtain the integral-equations in the frequency domain to solve scattering problems in three dimensions.

3.4 Integral equations for scattering by a single object

In this section we use the integral relations Eq. (3.28) and Eq. (3.29) from the previous section to derive the integral equations for scattering by a single object. The incident field that illuminates the object is generated by an external electric current density source. This situation is depicted in Figure 3.5. The electromagnetic properties of the medium $\overline{\mathcal{D}}$ and the object $\mathcal{D}$ will be given in the sections where the integral equations for a particular kind of object are derived.

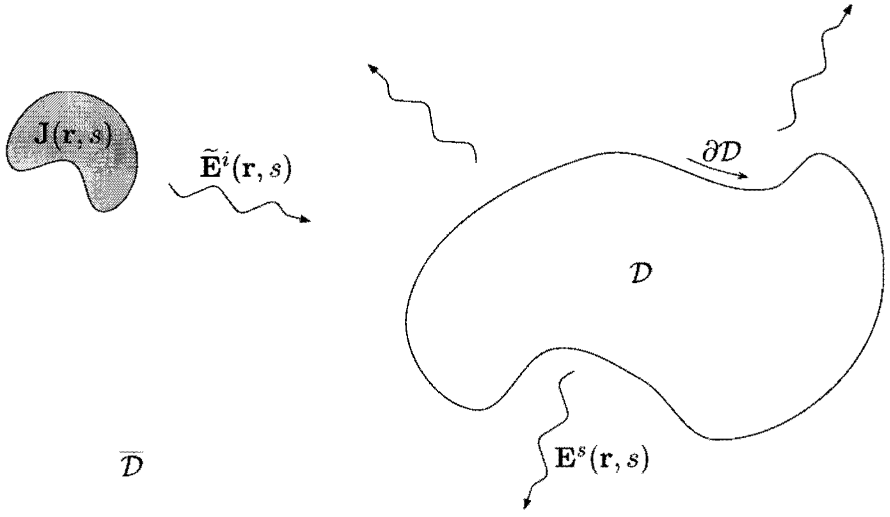

Figure 3.5: *Domain definitions for derivation of the integral equations.*

3.4.1 Scattering by an electrically impenetrable object

First, we consider the scattering by a single, electrically impenetrable object. As a point of departure we use Eqs. (3.28) - (3.29). We consider $\overline{\mathcal{D}}$ to consist of a homogenous, lossless dielectric space with constant permeability $\mu = \mu_0$ and constant permittivity $\epsilon = \epsilon_0$. The domain $\mathcal{D}$ is perfectly conducting and therefore electrically impenetrable. The scattered field has no sources in the exterior domain $\overline{\mathcal{D}}$. Therefore, the field intensities satisfy the equations

$$\nabla \times \mathbf{H}^s(\mathbf{r}, s) - s\epsilon_0 \mathbf{E}^s(\mathbf{r}, s) = \mathbf{0}, \tag{3.32}$$

$$\nabla \times \mathbf{E}^s(\mathbf{r}, s) + s\mu_0 \mathbf{H}^s(\mathbf{r}, s) = \mathbf{0}, \tag{3.33}$$

when $\mathbf{r} \in \overline{\mathcal{D}}$. Combining these equations with Eq. (3.28) leads to

$$\left\{-1, -\frac{1}{2}, 0\right\} \mathbf{H}^s(\mathbf{r}, s) \;=\; (s\mu_0)^{-1} \left(\nabla\nabla \cdot -\gamma_0^2\right) \boldsymbol{A}_B^{m,s}(\mathbf{r}, s) + \nabla \times \boldsymbol{A}_B^{e,s}(\mathbf{r}, s) \tag{3.34}$$

for $\mathbf{r} \in \{\overline{\mathcal{D}},\ \partial\mathcal{D},\ \mathcal{D}\}$. In Eq. (3.34), the potentials $\boldsymbol{A}_B$ are the ones defined in Eq. (3.30) and Eq. (3.31), while the additional superscript ^{s} refers to the fact that these potentials now pertain to the scattered field. Finally the minus sign in the left-hand side of Eq. (3.34) originates from the fact that $\mathbf{n}(\mathbf{r})$ points into $\overline{\mathcal{D}}$.

In writing down Eq. (3.34), we have applied the integral relation given by Eq. (3.28) to an infinite domain. Strictly speaking, this is not allowed, since this relation was derived for a finite domain only. However, we can also arrive at Eq. (3.34) by considering the domain between $\partial\mathcal{D}$ and a second boundary at $r = r_\infty$. From the radiation condition that the scattered field vanishes as $r \to \infty$ and $\mathrm{Re}(s) > 0$, it is seen that the contribution from this extra boundary vanishes by choosing a sufficiently large radius r_∞.

Next we consider the incident field in the interior $\mathcal{D}$. This field has its sources in $\overline{\mathcal{D}}$, therefore we have

$$\nabla \times \mathbf{H}^i(\mathbf{r}, s) - s\epsilon_0 \mathbf{E}^i(\mathbf{r}, s) = \mathbf{0}, \tag{3.35}$$

$$\nabla \times \mathbf{E}^i(\mathbf{r}, s) - s\mu_0 \mathbf{E}^i(\mathbf{r}, s) = \mathbf{0}, \tag{3.36}$$

when $\mathbf{r} \in \mathcal{D}$. As a consequence, Eq. (3.28) is reduced to

$$\left\{0, \frac{1}{2}, 1\right\} \mathbf{H}^i(\mathbf{r}, s) = \nabla \times \left[\boldsymbol{A}_B^{e,i}(\mathbf{r}, s) + \boldsymbol{A}_B^{m,i}(\mathbf{r}, s)\right], \tag{3.37}$$

for $\mathbf{r} \in \{\overline{\mathcal{D}},\ \partial\mathcal{D},\ \mathcal{D}\}$. Finally we already mentioned that the object is electrically impenetrable, which provides us with the boundary condition

$$\mathbf{J}_B^{m,i}(\mathbf{r}, s) + \mathbf{J}_B^{m,s}(\mathbf{r}, s) = \mathbf{J}_B^m(\mathbf{r}, s) = \mathbf{n}(\mathbf{r}) \times \mathbf{E}(\mathbf{r}, s) = \mathbf{0}, \tag{3.38}$$

when $\mathbf{r} \in \partial\mathcal{D}$. We end up with an integral relation involving only the magnetic-field strength $\mathbf{H}(\mathbf{r}, s)$ by adding Eqs. (3.34) and (3.37)

$$\left\{1, \frac{1}{2}, 0\right\} \mathbf{H}(\mathbf{r}, s) = \mathbf{H}^i(\mathbf{r}, s) - \nabla \times \boldsymbol{A}_B^e(\mathbf{r}, s), \tag{3.39}$$

for $\mathbf{r} \in \{\overline{\mathcal{D}},\ \partial\mathcal{D},\ \mathcal{D}\}$. Once the tangential magnetic field $\mathbf{n} \times \mathbf{H}(\mathbf{r}, s)$ is known on $\partial\mathcal{D}$, the normal components on $\partial\mathcal{D}$ and the field in $\overline{\mathcal{D}}$ are obtained directly by evaluating the term $\nabla \times \boldsymbol{A}_B^e(\mathbf{r}, s)$ in Eq. (3.39).

Analogous to Eq. (3.39) we derive for the electric-field component

$$\left\{1,\frac{1}{2},0\right\}\mathbf{E}(\mathbf{r},s)=\mathbf{E}^{i}(\mathbf{r},s)-(s\epsilon_0)^{-1}\left(\gamma_0^2-\nabla\nabla\cdot\right)\boldsymbol{A}_B^{e}(\mathbf{r},s), \tag{3.40}$$

for $\mathbf{r}\in\{\overline{\mathcal{D}},\ \partial\mathcal{D},\ \mathcal{D}\}$. Note that the last term in the right-hand side of Eq. (3.40) represents the scattered electric field.

In order to make Eqs. (3.39) – (3.40) suitable for numerical procedures, we still have to select the tangential field components on $\partial\mathcal{D}$, and we must evaluate the curl operation. In this case we take the cross-product with $\mathbf{n}(\mathbf{r})$, and solve the resulting integral equation for source density of electric surface current

$$\mathbf{J}_B^{e}(\mathbf{r},s)=-\mathbf{n}(\mathbf{r})\times\mathbf{H}(\mathbf{r},s). \tag{3.41}$$

With this definition and Eq. (3.27), Eq. (3.39) can be rewritten as

$$\mathbf{J}_B^{e}(\mathbf{r},s)=2\,\mathbf{J}_B^{e,i}(\mathbf{r},s)-2\,\mathbf{n}(\mathbf{r})\times\nabla\times\boldsymbol{A}_B^{e}(\mathbf{r},s). \tag{3.42}$$

In the literature, Eq. (3.42) is known as the magnetic-field integral equation (MFIE). Since it pertains to field values on $\partial\mathcal{D}$, it is of the boundary type. A similar integral equation can be obtained by considering the electric-field strength $\mathbf{E}(\mathbf{r},s)$ for $\mathbf{r}\in\partial\mathcal{D}$, and is known as the electric-field integral equation (EFIE)

$$[\mathbf{n}(\mathbf{r})\times\nabla]\nabla\cdot\boldsymbol{A}_B^{e}(\mathbf{r},s)-\gamma_0^2\,\mathbf{n}(\mathbf{r})\times\boldsymbol{A}_B^{e}(\mathbf{r},s)+(s\epsilon_0)\mathbf{J}_B^{m,i}(\mathbf{r},s)=\mathbf{0}. \tag{3.43}$$

This EFIE is of the first kind, which makes it less suitable for a numerical solution. An integral equation is called of the first kind if the observable is only inside the integral in the equation (e.g. $\mathbf{J}_B^{e}(\mathbf{r},s)$ occurs only in the vector potential in Eq. (3.43)) and of the second kind if the observable occurs explicitly outside the integral (e.g. in the MFIE $\mathbf{J}_B^{e}(\mathbf{r},s)$ occurs in both the left-hand side and the vector potential).

The last term in the right-hand side of Eq. (3.42) will be observed a bit closer now. We first rewrite this term as

$$\begin{aligned}\mathbf{n}(\mathbf{r})\times\nabla\times\boldsymbol{A}_B^{e}(\mathbf{r},s)&=\mathbf{n}(\mathbf{r})\times\nabla\times\oint_{\mathbf{r}'\in\partial\mathcal{D}}\underbrace{\frac{\exp(-\gamma_0|\mathbf{r}-\mathbf{r}'|)}{|\mathbf{r}-\mathbf{r}'|}}_{G(\mathbf{r}-\mathbf{r}',s)}\mathbf{J}_B^{e}(\mathbf{r}',s)d\mathbf{r}'\\&=\oint_{\mathbf{r}'\in\partial\mathcal{D}}\mathbf{n}(\mathbf{r})\times\nabla\times\left[G(\mathbf{r}-\mathbf{r}',s)\,\mathbf{J}_B^{e}(\mathbf{r}',s)\right]d\mathbf{r}'.\end{aligned} \tag{3.44}$$

Next we carry out the curl operation, where we make use of the identities

$$\nabla\left[\frac{1}{|\mathbf{r}-\mathbf{r}'|}\right]=-\frac{\mathbf{r}-\mathbf{r}'}{|\mathbf{r}-\mathbf{r}'|^3}, \tag{3.45}$$

$$\nabla\left[\exp(-\gamma_0|\mathbf{r}-\mathbf{r}'|)\right]=-\gamma_0\frac{\mathbf{r}-\mathbf{r}'}{|\mathbf{r}-\mathbf{r}'|}\exp(-\gamma_0|\mathbf{r}-\mathbf{r}'|), \tag{3.46}$$

and the fact that $\nabla\times\mathbf{J}_B^{e}(\mathbf{r}',s)=\mathbf{0}$. Eq. (3.42) now becomes

$$\mathbf{J}_B^{e}(\mathbf{r},s)=2\mathbf{J}_B^{e,i}(\mathbf{r},s)-2\oint_{\mathbf{r}'\in\partial\mathcal{D}}\left[\gamma_0+\frac{1}{|\mathbf{r}-\mathbf{r}'|}\right]G(\mathbf{r}-\mathbf{r}',s)\,[\mathbf{n}(\mathbf{r})\times\mathbf{J}_B^{e}(\mathbf{r}',s)\times\mathbf{u}_R]d\mathbf{r}', \tag{3.47}$$

where $\mathbf{u}_R = (\mathbf{r}-\mathbf{r}')/|\mathbf{r}-\mathbf{r}'|$ is the unit vector in the direction from the source point $\mathbf{r}'$ towards the observation point $\mathbf{r}$. The MFIE is now suitable for use in various numerical procedures. The EFIE can be written in a similar form. We leave this out of consideration here, since we derive a special form of the EFIE for thin wires further on in this report.

3.4.2 Scattering by a lossy dielectric object

We now consider the case where $\overline{\mathcal{D}}$ in Figure 3.5 is the same as in the impenetrable case and $\mathcal{D}$ contains an inhomogeneous dielectric with constant permeability $\mu(\mathbf{r}) \geq \mu_0$, permittivity $\epsilon(\mathbf{r}) \geq \epsilon_0$ and $\sigma(\mathbf{r}) \geq 0$. For this configuration Maxwell's equations satisfy

$$\nabla \times \mathbf{E}(\mathbf{r},s) + s\mu(\mathbf{r})\mathbf{H}(\mathbf{r},s) = \mathbf{J}^m(\mathbf{r},s), \tag{3.48}$$

$$\nabla \times \mathbf{H}(\mathbf{r},s) - s\epsilon(\mathbf{r})\mathbf{E}(\mathbf{r},s) = \sigma(\mathbf{r})\mathbf{E}(\mathbf{r},s) + \mathbf{J}^e(\mathbf{r},s), \tag{3.49}$$

for $\mathbf{r} \in \mathbb{R}^3$. The scattered field can be obtained by subtracting the incident field from these last two equations. The incident field satisfies

$$\nabla \times \mathbf{E}^i(\mathbf{r},s) + s\mu_0\mathbf{H}^i(\mathbf{r},s) = \mathbf{J}^m(\mathbf{r},s), \tag{3.50}$$

$$\nabla \times \mathbf{H}^i(\mathbf{r},s) - s\epsilon_0\mathbf{E}^i(\mathbf{r},s) = \mathbf{J}^e(\mathbf{r},s). \tag{3.51}$$

Subtracting the incident field equations Eqs. (3.50) – (3.51) from Eqs. (3.48) – (3.49) gives

$$\nabla \times \mathbf{E}^s(\mathbf{r},s) + s\mu_0\mathbf{H}^s(\mathbf{r},s) = \mathbf{J}^m_D(\mathbf{r},s), \tag{3.52}$$

$$\nabla \times \mathbf{H}^s(\mathbf{r},s) - s\epsilon_0\mathbf{E}^s(\mathbf{r},s) = \mathbf{J}^e_D(\mathbf{r},s), \tag{3.53}$$

where the contrast current densities are defined as

$$\mathbf{J}^m_D(\mathbf{r},s) = s\left[\mu(\mathbf{r}) - \mu_0\right]\mathbf{H}(\mathbf{r},s), \tag{3.54}$$

$$\mathbf{J}^e_D(\mathbf{r},s) = s\left[\Big(\epsilon(\mathbf{r}) - \epsilon_0\Big) + \frac{\sigma(\mathbf{r})}{s}\right]\mathbf{E}(\mathbf{r},s). \tag{3.55}$$

We now have a system of equation that provides the solution of both the magnetic and electric field. The sources that generate the electromagnetic field are in this case the contrast current densities.

By definition, $\mu(\mathbf{r}) = \mu_0$ and hence, the magnetic contrast current density equals zero. On account of the scattered field equations, Eq. (3.28) and Eq. (3.29) lead to

$$\mathbf{H}^s(\mathbf{r},s) = \nabla \times \boldsymbol{A}_D(\mathbf{r},s), \tag{3.56}$$

$$\mathbf{E}^s(\mathbf{r},s) = (s\epsilon_0)^{-1}\left(\nabla\nabla\cdot - \gamma_0^2\right)\boldsymbol{A}_D(\mathbf{r},s), \tag{3.57}$$

with $\gamma_0^2 = s^2\mu_0\epsilon_0$ and $\mathbf{r} \in \mathcal{D}$. Since we only have a vector potential of the electric type we omitted the superscript ^{e} here.

3.5 Coupling between two objects

Since the objects show no magnetic contrast, it is sufficient to solve the coupling problem for the electric field only in the analysis of two mutually coupled objects. From Eq. (3.29) it follows that the scattered fields generated by the objects A and B are

$$\mathbf{E}^s_A(\mathbf{r},s) = (s\epsilon_0)^{-1}\left(\nabla\nabla\cdot - \gamma_0^2\right)\mathbf{A}^s_{D,A}(\mathbf{r},s), \text{ for } \mathbf{r}\in\mathcal{D}_A \text{ or } \partial\mathcal{D}_A, \tag{3.58}$$

$$\mathbf{E}^s_B(\mathbf{r},s) = (s\epsilon_0)^{-1}\left(\nabla\nabla\cdot - \gamma_0^2\right)\mathbf{A}^s_{D,B}(\mathbf{r},s), \text{ for } \mathbf{r}\in\mathcal{D}_B \text{ or } \partial\mathcal{D}_B, \tag{3.59}$$

with

$$\mathbf{A}^s_{D,A}(\mathbf{r},s) = \int_{\mathbf{r}'\in\mathcal{D}_A} G(\mathbf{r}-\mathbf{r}',s)\mathbf{J}_A(\mathbf{r}',s)d\mathbf{r}',$$

$$\mathbf{A}^s_{D,B}(\mathbf{r},s) = \int_{\mathbf{r}''\in\mathcal{D}_B} G(\mathbf{r}-\mathbf{r}'',s)\mathbf{J}_B(\mathbf{r}'',s)d\mathbf{r}'',$$

in which the extra subscripts $_A$ and $_B$ refer to object A and object B, respectively. For our convenience we rewrite Eqs. (3.58) – (3.59) in a symbolic form

$$\mathbf{E}^s_A = \mathcal{K}_A\mathbf{E}_A, \tag{3.60}$$

$$\mathbf{E}^s_B = \mathcal{K}_B\mathbf{E}_B. \tag{3.61}$$

This leaves two simple equations to work with.

To determine the coupling between two objects, we need expressions for the scattered field in $\overline{\mathcal{D}}$, since this is a part of the total incident field that illuminates a second object. To obtain these expressions, we decompose the total electromagnetic field $\{\mathbf{E}(\mathbf{r},s),\mathbf{H}(\mathbf{r},s)\}$ into the incident field $\{\mathbf{E}^i(\mathbf{r},s),\mathbf{H}^i(\mathbf{r},s)\}$ and the scattered field $\{\mathbf{E}^s(\mathbf{r},s),\mathbf{H}^s(\mathbf{r},s)\}$. The total field of an object can than be written as the sum of the scattered and the total incident field as was demonstrated earlier in this chapter. Note that the total incident field is composed of an incident field $\tilde{\mathbf{E}}^i$ and a scattered field from, in this problem, a second object.

We will now make use of the simplified expressions for the electric fields Eqs. (3.60) – (3.61) to compose two coupled integral equations. To do so, we substitute the total incident field for object A, $\mathbf{E}^i_A = \mathbf{E}^s_B + \tilde{\mathbf{E}}^i$ in $\mathbf{E}_A = \mathbf{E}^i_A + \mathbf{E}^s_A$ and a similar expression for the incident field of object B in $\mathbf{E}_B = \mathbf{E}^i_B + \mathbf{E}^s_B$, where $\tilde{\mathbf{E}}^i$ is the incident field excited by the current source located in $\overline{\mathcal{D}}$. Next we substitute this in the simplified equations Eqs. (3.60) – (3.61). This yields

$$\left.\begin{array}{ll}\mathbf{E}_A = \tilde{\mathbf{E}}^i + \mathcal{K}_B\mathbf{E}_B + \mathcal{K}_A\mathbf{E}_A, & \mathbf{r}\in\mathcal{D}_A\\ \mathbf{E}_B = \tilde{\mathbf{E}}^i + \mathcal{K}_A\mathbf{E}_A + \mathcal{K}_B\mathbf{E}_B, & \mathbf{r}\in\mathcal{D}_B\end{array}\right\} \Rightarrow \left\{\begin{array}{l}(\mathcal{K}_A - I)\mathbf{E}_A + \mathcal{K}_B\mathbf{E}_B = -\tilde{\mathbf{E}}^i\\ \mathcal{K}_A\mathbf{E}_A + (\mathcal{K}_B - I)\mathbf{E}_B = -\tilde{\mathbf{E}}^i\end{array}\right., \tag{3.62}$$

where I is the identity operator. These equations can be cast in the following matrix-operator form

$$\begin{bmatrix}\mathcal{K}_A - I & \mathcal{K}_B\\ \mathcal{K}_A & \mathcal{K}_B - I\end{bmatrix}\begin{bmatrix}\mathbf{E}_A\\ \mathbf{E}_B\end{bmatrix} = \begin{bmatrix}-\tilde{\mathbf{E}}^i\\ -\tilde{\mathbf{E}}^i\end{bmatrix}. \tag{3.63}$$

The matrix-operator form Eq. (3.63) applies to any problem which involves electromagnetic coupling between two dielectric objects. A similar form can be derived for coupling between a dielectric and a conducting body, or between two conducting bodies. When the EFIE is used to determine the current on the surface of the conducting body, the identity operator I is not present in the corresponding operator on the diagonal. This will be seen for specific cases further on in this report.

Chapter 4

Two wires in free space

In this chapter, we use the previously described technique (see Eq. (3.63)) to formulate a matrix operator that describes the electromagnetic behavior of two electromagnetically coupled wires. This system will be solved with the aid of the WCG-FFT (Weak Conjugate-Gradient - Fast Fourier-Transformation) technique, which will be described later.
We determine the integral representation for the field radiated by an antenna in two different manners. These equations will then be written in a general form and finally cast in a matrix operator as was proposed in the previous chapter. Of course the solutions to the integral equations for the antennas will be validated with independent results later on in this report. The scattered field remains in its strong form here. The weak form mentioned earlier will be developed in Chapter 6.

4.1 Scattering by a single thin wire

We consider a wire of length L and radius a positioned along the z-axis from $z = -L/2$ to $z = L/2$ (see Figure 4.1). The wire is embedded in vacuum. We will derive two integral equations to solve the scattering problem. The first integral equation pertains to a classical configurations with infinite conductivity and the second approach handles a wire with finite conductivity.

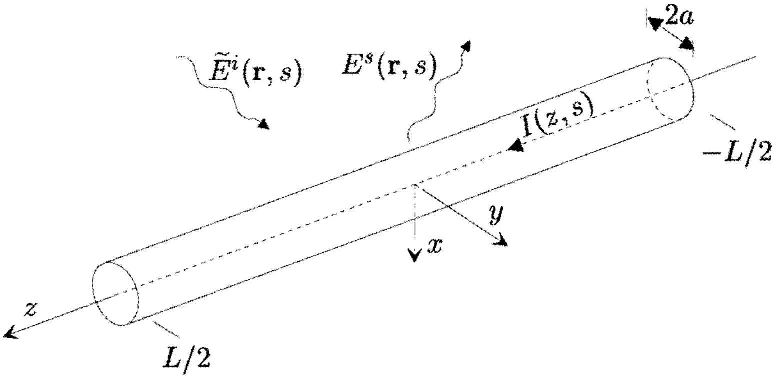

Figure 4.1: *Wire geometry*

In the previous chapter, we have derived an electric field representation (see Eq. (3.40)) that handles the scattering of electromagnetic waves by an electrically impenetrable object. From this equation we now derive a convenient integral equation to evaluate the current along the wire. The result is also known as Pocklington's integral equation. The second integral equation follows directly from evaluating the domain vector potential in Eq. (3.29). This equation describes the scattering by a lossy dielectric object. It may be applied here when the wire is no longer perfectly conducting, and the electromagnetic field therefore penetrates into the wire. Note that the vector potential in the impenetrable case is of the boundary type and that the vector potential in the penetrable case involves the entire domain of the wire.

4.2 The integral equations of Pocklington

As point of departure, we use Eq. (3.29). We first consider the scattered field outside the wire, i.e., in $\overline{\mathcal{D}}$. To compute this field efficiently, we need a good approximation of the boundary vector potential Eq. (3.31) used in Eq. (3.29)

$$\boldsymbol{A}^{e}_{B}(\mathbf{r},s) = \oint_{\mathbf{r}'\in\partial\mathcal{D}} G(R,s)\mathbf{J}_{B}(\mathbf{r}',s)d\mathbf{r}',$$

with

$$G(R,s) = \frac{\exp(-\gamma_0 R)}{4\pi R}, \tag{4.1}$$

and $R = |\mathbf{r}-\mathbf{r}'|$ for the case where $R >> a$ for all source points $\mathbf{r}'$ on the wire. To facilitate the formulation, we introduce cylindrical coordinates according to $\mathbf{r}' = z'\mathbf{u}_{z'} + \rho'\mathbf{u}_{\rho'} = z'\mathbf{u}_z + \rho'\mathbf{u}_{\rho'}$ and $\mathbf{r} = z\mathbf{u}_z + \rho\mathbf{u}_\rho$. For $\mathbf{r}'$ on the surface of the wire and $\mathbf{r}$ in the exterior domain, R can be written as

$$R = \sqrt{|\mathbf{r} - z'\mathbf{u}_z|^2 + \rho'^2 - 2a\ \mathbf{u}_{\rho'}\cdot(\mathbf{r} - z'\mathbf{u}_z)}. \tag{4.2}$$

We carry out a Taylor expansion in terms of $a/|\mathbf{r} - z'\mathbf{u}_z|$ in Eq. (4.2), we obtain

$$R = |\mathbf{r} - z'\mathbf{u}_z| - \frac{a\ \mathbf{u}_{\rho'}\cdot(\mathbf{r} - z'\mathbf{u}_z)}{|\mathbf{r} - z'\mathbf{u}_z|} + \mathcal{O}\left(a^2/R^2\right). \tag{4.3}$$

As can be seen we obtain second-order accuracy due to the error term $\mathcal{O}(a^2/R^2)$. Next, we rewrite Green's function as

$$\begin{aligned} G(R,s) &= G(R_0,s) - \frac{a\ \mathbf{u}_{\rho'}\cdot(\mathbf{r} - z'\mathbf{u}'_z)}{R_0}\ \frac{\partial}{\partial R}G(R,s)\Big|_{R=R_0} \\ &= G(R_0,s) - \Delta G(R_0,s), \end{aligned} \tag{4.4}$$

with $R_0 = |\mathbf{r} - z'\mathbf{u}_z|$. The current density can be decomposed into two components

$$\mathbf{J}_B(\mathbf{r}',s) = J_\phi(\mathbf{r}',s)\mathbf{u}_{\phi'} + J_z(\mathbf{r}',s)\mathbf{u}_z. \tag{4.5}$$

First we consider the ϕ-component of the current density. The ϕ-component can be rewritten as

$$J_\phi(\mathbf{r}',s) = \overline{J}_\phi(z',s) + \left[J_\phi(\mathbf{r}',s) - \overline{J}_\phi(z',s)\right] = \overline{J}_\phi(z',s) + \Delta J_\phi(\mathbf{r}',s), \tag{4.6}$$

where the average value of J_ϕ is defined as

$$\overline{J}_\phi(z',s) = \frac{1}{2\pi}\int_{-\pi}^{\pi} J_\phi(z'\mathbf{u}_z + a\,\mathbf{u}_{\rho'}, s)d\phi'. \tag{4.7}$$

If we substitute Eq. (4.7) in the boundary vector potential, the contribution of the current density $J_\phi(\mathbf{r},s)$ in this vector potential becomes

$$\begin{aligned}
&\int_{-\pi}^{\pi} a\; d\phi' \left[G(R,s)J_\phi(\mathbf{r}',s)\mathbf{u}_{\phi'}\right] = \\
&\qquad \int_{-\pi}^{\pi} a\; d\phi' \Bigg[\underbrace{G(R_0,s)\overline{J}_\phi(z',s)\mathbf{u}_{\phi'}}_{0} - \underbrace{\Delta G(R_0,s)\Delta J_\phi(\mathbf{r}',s)\mathbf{u}_{\phi'}}_{\mathcal{O}(a^2)} - \\
&\qquad\qquad \underbrace{\Delta G(R_0,s)\overline{J}_\phi(z',s)\mathbf{u}_{\phi'} + G(R_0,s)\Delta J_\phi(\mathbf{r}',s)\mathbf{u}_{\phi'}}_{\mathcal{O}(a)}\Bigg].
\end{aligned} \tag{4.8}$$

The first term becomes zero after integration because $\int_{-\pi}^{\pi} d\phi'\mathbf{u}_{\phi'} = 0$ and the second term is negligible because it is of $\mathcal{O}(a^2)$. We cannot lose the last two terms through integration because $\mathbf{u}_{\phi'}$ depends on ϕ'. We can, however, estimate them as being of $\mathcal{O}(a)$. This means that the current density $J_\phi(\mathbf{r}',s)$ can be neglected in the total boundary current $J_B^e(\mathbf{r},s)$ up to $\mathcal{O}(a)$. For this reason, it is sufficient to look at the z-component of the current density to determine the boundary vector potential. A similar approach can be followed for the z-component of $\mathbf{J}(\mathbf{r}',s)$. In this case we also write $J_z(\mathbf{r}',s)$ as

$$J_z(\mathbf{r}',s) = \overline{J}_z(\mathbf{r}',s) + \left[J_z(\mathbf{r}',s) - \overline{J}_z(\mathbf{r}',s)\right] = \overline{J}_z(\mathbf{r}',s) + \Delta J_z(\mathbf{r}',s), \tag{4.9}$$

where the averaged J_z is defined as

$$\overline{J}_z(z',s) = \frac{1}{2\pi}\int_{-\pi}^{\pi} J_z(z'\mathbf{u}_z + a\mathbf{u}_{\rho'}, s)\; d\phi'. \tag{4.10}$$

If we now substitute Eq. (4.9) in the boundary vector potential, the contribution of the current density $J_z(\mathbf{r}',s)$ in this vector potential becomes

$$\begin{aligned}
&\int_{-\pi}^{\pi} a\; d\phi' \left[G(R,s)J_z(\mathbf{r}',s)\mathbf{u}_{\phi'}\right] = \\
&\qquad \int_{-\pi}^{\pi} a\; d\phi' \Bigg[G(R_0,s)\overline{J}_z(\mathbf{r}',s)\mathbf{u}_{\phi'} - \underbrace{\Delta G(R_0,s)\Delta J_z(\mathbf{r}',s)\mathbf{u}_{\phi'}}_{\mathcal{O}(a^2)} - \\
&\qquad\qquad \underbrace{\Delta G(R_0,s)\overline{J}_z(\mathbf{r}',s)\mathbf{u}_{\phi'}}_{0} + \underbrace{G(R_0,s)\Delta J_z(\mathbf{r}',s)\mathbf{u}_{\phi'}}_{0}\Bigg].
\end{aligned} \tag{4.11}$$

We observe that in the right-hand side of Eq. (4.11) the last two terms become zero through integration and the second term in the right-hand side is of $\mathcal{O}(a^2)$ and is therefore negligible. If we substitute the remainder of Eq. (4.11) in Eq. (3.29), we obtain

$$\mathbf{E}(\mathbf{r},s) = (s\epsilon_0)^{-1}(\nabla\partial_z - \gamma_0^2\mathbf{u}_z)\int_{-L/2}^{L/2} G(R_0,s)\; a\overline{J}_z(\mathbf{r}',s)\int_{-\pi}^{\pi} d\phi' dz', \tag{4.12}$$

which is now completely determined by the total current $I(z's)$, which is concentrated on the z-axis. This current is defined as

$$I(z', s) = a \int_{-\pi}^{\pi} J_z(z'\mathbf{u}_z + a\mathbf{u}_{\rho'}, s)d\phi' = a \int_{-\pi}^{\pi} \overline{J}_z(z', s)d\phi'. \tag{4.13}$$

With this definition Eq. (4.12) reduces to:

$$\mathbf{E}(\mathbf{r}, s) = (s\epsilon_0)^{-1}(\nabla\partial_z - \gamma_0^2\mathbf{u}_z) \int_{-L/2}^{L/2} G(R_0, s)I(z', s)dz' + \mathcal{O}(a). \tag{4.14}$$

From this result, we observe that the scattered field is almost completely determined by the total current along the wire. In case of a delta-gap voltage excitation, the input impedance of the antenna is determined by the value of this current at the location of the gap. Therefore, it would be more efficient if an integral equation for this current can be derived.

To obtain such an equation, we return to the integral representation Eq. (3.59), and we consider the z-component of this equation for $\mathbf{r}$ on the central axis of the cylinder. We then obtain the following expression

$$\begin{aligned} s\epsilon_0 E_z^s(z\mathbf{u}_z, s) &= \nabla\partial_z \oint_{\mathbf{r}'\in\partial\mathcal{D}} G(R, s)\mathbf{J}_B(\mathbf{r}', s)d\mathbf{r}' - \\ &\quad \gamma_0^2 \oint_{\mathbf{r}'\in\partial\mathcal{D}} G(R, s)J_z(z'\mathbf{u}_z + a\mathbf{u}_{\rho'}, s)d\mathbf{r}', \end{aligned} \tag{4.15}$$

with $R = |\mathbf{r} - z'\mathbf{u}_z|$. As can be observed from Eq. (4.15), we still have the $\nabla\cdot$ operator in our equation. We can decompose this divergence into two operators, namely a z component $\partial_z\mathbf{u}_z$ and a transversal component $\nabla_{\mathrm{T}}\cdot$. We first discuss the transversal part of the divergence in Eq. (4.15). This part can be written as

$$\nabla_{\mathrm{T}} \cdot \oint_{\mathbf{r}'\in\partial\mathcal{D}} G(R, s)\mathbf{J}_B(\mathbf{r}', s)d\mathbf{r}' = \oint_{\mathbf{r}'\in\partial\mathcal{D}} \mathbf{J}_B(\mathbf{r}', s)\nabla_{\mathrm{T}} \cdot G(R, s)\mathbf{r}'. \tag{4.16}$$

After applying the $\nabla_{\mathrm{T}}\cdot$ operator, Eq. (4.16) becomes

$$\oint_{\mathbf{r}'\in\partial\mathcal{D}} \mathbf{J}_B(\mathbf{r}', s) \cdot \frac{a\ \mathbf{u}_{\rho'}}{|\mathbf{r} - \mathbf{r}'|} \frac{\partial}{\partial R} G(R, s)d\mathbf{r}', \tag{4.17}$$

where we already made use of the fact that on the z-axis $\rho = 0$. Since $\mathbf{J}_B(\mathbf{r}, s)\perp\mathbf{u}_{\rho'}$, the inner product between $\mathbf{J}_B$ and $\mathbf{u}_{\rho'}$ is zero. This means that the part of Eq. (4.15) that was isolated in Eq. (4.16) vanishes, provided that we neglect the end effects of the current on the wire. We can now write Eq. (4.15) as

$$\begin{aligned} s\epsilon_0 E_z^s(z\mathbf{u}_z, s) &= \left(\partial_z^2 - \gamma_0^2\right) \int_{-L/2}^{L/2} G(z - z', s) \int_{-\pi}^{\pi} J_z(z'\mathbf{u}_z + a\mathbf{u}_{\rho'}, s)a d\phi' dz', \\ G(z, s) &= \frac{\exp(-\gamma_0 R_a)}{4\pi R_a}, \end{aligned} \tag{4.18}$$

with $L/2 \leq z \leq L/2$ and $R_a = \sqrt{z^2 + a^2}$. In Eq. (4.18) the integral over ϕ' can be recognized as the total current $I(z', s)$, which is concentrated on the z-axis (see Eq. (4.10)). With the definition of the current $I(z', s)$ we end up with the approximate integro-differential equation of Pocklington

$$s\epsilon_0 E_z^s(z\mathbf{u}_z, s) = (\partial_z^2 - \gamma_0^2) \int_{-L/2}^{L/2} G(z - z', s) I(z', s) dz', \tag{4.19}$$

$$G(z, s) = \frac{\exp(-\gamma_0 R_a)}{4\pi R_a}. \tag{4.20}$$

From the above derivation, which was first given in [31], it follows that this integral equation is almost exact. In fact, the only approximation amounts to neglecting the equation for the radial current on the end faces.

The numerical solution of the integral equation for a single wire Eq. (4.19) has already been implemented in several programs. In the present study, the implementation of [19] has been used as a starting point. The current distribution is calculated by exciting the wire with a plane wave and using the boundary condition $E_z^i(z\mathbf{u}_z, s) = -E_z^s(z\mathbf{u}_z, s)$. This leaves us with

$$-s\epsilon_0 E_z^i(z, s) = (\partial_z^2 - \gamma_0^2) \int_{-L/2}^{L/2} G(z - z', s) I(z', s) dz'. \tag{4.21}$$

We modified this program for a delta-gap source. With this modification, Eq. (4.21) becomes

$$-s\epsilon_0 V_{\mathrm{gap}} \delta(z - z_{\mathrm{gap}}) = (\partial_z^2 - \gamma_0^2) \int_{-L/2}^{L/2} G(z - z', s) I(z', s) dz', \tag{4.22}$$

where V_{gap} is a voltage source which is located at z_{gap} on the wire. Normally z_{gap} is chosen in the middle of the wire.

4.3 Integral equations for a wire with finite conductivity

The integral equation proposed by Pocklington is only appropriate for perfectly conducting wires. However, we want to tackle wires with finite conductivity as well. To formulate another set of equations with this vector potential, we need to prove that the major part of the current flows in the z-direction of the wire. As a short introduction we refer to the intermezzo given below.

4.3.1 Intermezzo

To formulate an alternative expression from which the total current in a wire can be solved, we need to prove that the internal electric field components normal to the surface are negligible compared to the other field components present. This implies that a current flowing in the radial direction from the surface towards the central axis of the wire must be sufficiently small. Such a current will be referred to as a radial current. To demonstrate this, we need expressions for the currents tangential to the surface of the wire, which will be referred to as tangential currents, and the radial current inside the wire. The first current mentioned above corresponds to the magnetic-field component tangential to the surface of the wire, and the electric-field component tangential to the surface of the wire multiplied by the conductivity.

We first assume that the field inside the wire behaves as a TM mode present in a circular waveguide. The TM-field is composed of $\{E_\rho,\ E_z,\ H_\phi\}\exp(st-\gamma z)$, where H_ϕ and E_z are indeed the tangential field components and where E_ρ is the normal field component mentioned above. These three field components depend solely on ρ. The symbol γ in the exponent denotes the axial propagation coefficient in the z-direction and the minus sign implies that the current flows in the positive z-direction. The propagation coefficient follows from solving an eigenvalue equation, which we derive later in this section. However we do not need an exact expression for γ to show that the radial current in the wire is negligible.
Substituting the TM-field components in Maxwell's equations and carrying out the curl operation yields three scalar equations for the nonvanishing field components, namely

$$\gamma H_\phi - (\sigma + s\epsilon)E_\rho = 0, \tag{4.23}$$

$$(\rho^{-1} + \partial_\rho)H_\phi - (\sigma + s\epsilon)E_z = 0, \tag{4.24}$$

$$-\gamma E_\rho + s\mu H_\phi - \partial_\rho E_z = 0. \tag{4.25}$$

Now Eq. (4.23) is rewritten as

$$E_\rho = \frac{\gamma}{\sigma + s\epsilon} H_\phi. \tag{4.26}$$

Substituting this result in Eq. (4.25) yields

$$H_\phi = \frac{\sigma + s\epsilon}{\kappa^2}\partial_\rho E_z, \tag{4.27}$$

with $\kappa^2 = s\mu(s\epsilon + \sigma) - \gamma^2$. Finally, substituting Eq. (4.27) in Eq. (4.24) yields

$$\rho^2\partial_\rho^2 E_z + \rho\partial_\rho E_z - (\kappa\rho)^2 E_z = 0. \tag{4.28}$$

This differential equation has two linearly independent solutions being $I_0(\kappa\rho)$, the modified Bessel function of the first kind and order zero, and $K_0(\kappa\rho)$, the modified Bessel function of the second kind and order zero. The modified Bessel function $I_0(\kappa\rho)$ is bounded at $\rho = 0$, whereas $K_0(\kappa\rho)$ is not. Under the assumption that the electric field at the boundary of the wire is represented by C_i, the electric field in the interior of the wire is given by

$$E_{z,i} = C_i\frac{I_0(\kappa_i\rho)}{I_0(\kappa_i a)}, \tag{4.29}$$

and in a similar way, the electric field exterior to the wire follows from

$$E_{z,e} = C_e\frac{K_0(\kappa_e\rho)}{K_0(\kappa_e a)}. \tag{4.30}$$

Applying the continuity condition $\lim_{\rho\uparrow a} E_{z,i} = \lim_{\rho\downarrow a} E_{z,e}$ leads to $C_i = C_e = C$. The magnitude of C only depends on the incident field. In view of Eq. (4.27) the corresponding H_ϕ-field in the interior is given by

$$H_{\phi,i} = C\,\frac{\sigma_i + s\epsilon_i}{\kappa_i}\,\frac{\partial_{\kappa_i\rho} I_0(\kappa_i\rho)}{I_0(\kappa_i a)}, \tag{4.31}$$

and in in a similar way, the magnetic field exterior to the wire follows from

$$H_{\phi,e} = C\,\frac{\sigma_e + s\epsilon_e}{\kappa_e}\,\frac{\partial_{\kappa_e\rho} K_0(\kappa_e\rho)}{K_0(\kappa_e a)}. \tag{4.32}$$

Enforcing the continuity of the tangential magnetic field components at $\rho = a$ leads to the eigenvalue equation mentioned earlier:

$$\frac{\sigma_i + s\epsilon_i}{\kappa_i} \frac{\partial_{\kappa_i a} I_0(\kappa_i a)}{I_0(\kappa_i a)} = \frac{\sigma_e + s\epsilon_e}{\kappa_e} \frac{\partial_{\kappa_e a} K_0(\kappa_e a)}{K_0(\kappa_e a)}. \tag{4.33}$$

By now we look at the Bessel functions a bit closer. In particular we are interested in their asymptotic behavior. Suppose that the conductivity approaches infinity, then the argument $\kappa_i \rho|_{\rho=a} \to \infty$ as long as $s > 0$. In that case the following asymptotic behavior of the Bessel functions is observed

$$I_0(\kappa\rho) \approx \sqrt{\frac{1}{2\pi\kappa\rho}} \exp(\kappa\rho), \tag{4.34}$$

$$K_0(\kappa\rho) \approx \sqrt{\frac{\pi}{\kappa\rho}} \exp(-\kappa\rho), \tag{4.35}$$

$$\partial_{\kappa\rho} I_0(\kappa\rho) \approx I_0(\kappa\rho), \tag{4.36}$$

$$\partial_{\kappa\rho} K_0(\kappa\rho) \approx -K_0(\kappa\rho). \tag{4.37}$$

To get some insight in the behavior of the axial propagation constant γ, we assume that γ is fixed and almost perfect conductivity for the wire ($\sigma_i \to \infty$). We then have $\kappa_i \sim \sqrt{\sigma_i}$ as $\sigma_i \to \infty$ and we can apply the asymptotic approximations for the Bessel function of the first kind to Eq. (4.33). Now from the fact that K_0 has no zeros and that $K_0' = -K_1$ has no poles in the right half of the complex argument plane, we have

$$\frac{\kappa_e}{s\epsilon_e} = 0. \tag{4.38}$$

Therefore we find that that $\kappa_e = 0$. This is in agreement with the condition to use the limiting form of the modified Bessel function of the second kind. With $\kappa_e = 0$ we find that $\gamma^2 = s^2\mu\epsilon_e$, which is consistent with the assumption that γ has a fixed value.

Based on the field components that are known, we obtain the radial and tangential current density in the wire by multiplying the electric field components with the conductivity as follows

$$J_\rho = C \frac{\sigma\gamma}{\kappa_i} \frac{\partial_{\kappa_i \rho} I_0(\kappa_i \rho)}{I_0(\kappa_i a)}, \tag{4.39}$$

$$J_z = C\sigma \frac{I_0(\kappa_i \rho)}{I_0(\kappa_i a)}. \tag{4.40}$$

Next we write the radial current density in terms of the tangential current density by eliminating C. This yields

$$J_\rho = \frac{\gamma}{\kappa_i} \frac{\partial_{\kappa_i \rho} I_0(\kappa_i \rho)}{I_0(\kappa_i \rho)} J_z. \tag{4.41}$$

For a wire with perfect conductivity we observed that γ^2 equals $s^2\epsilon_e\mu$ and $\kappa_i \to \infty$. A wire with a finite conductivity, still has a large value for the conductivity. In particular the factor $s\mu\sigma_i$ is much larger than $s^2\epsilon_e\mu$. Therefore we can still use the asymptotic approximations for the modified Bessel functions.

With $\kappa_i >> \gamma$, we may now conclude that the radial current is negligible compared to the tangential current.

4.3.2 Scattered field for a wire with finite conductivity

From Eq. (4.40) it is observed that the tangential current J_z is not constant over the entire domain of integration for wires with a finite conductivity. We have also observed that κ_i is very large for a wire with a finite conductivity. The current density inside the wire is composed of an amplitude corresponding to the current density on the surface of the wire and a quantity which governs the penetration into the wire of the tangential current. The current distribution inside the wire is expressed by the quantity

$$W(\rho) = \frac{I_0(\xi)}{I_0(\xi_0)}, \tag{4.42}$$

which denotes the ratio of current density at any internal point r to the current density at the surface. Here $\xi = \rho\sqrt{s\mu_0\sigma}$ and $\xi_0 = a\sqrt{s\mu_0\sigma}$, where both ξ and ξ_0 have to be large enough to justify the use of the asymptotic approximations Eqs. (4.34) - (4.37). With the aid of these approximations $W(\rho)$ can be determined as

$$W(\rho) = \sqrt{a/\rho}\exp\left[-(a-\rho)/\delta\right], \tag{4.43}$$

where

$$\delta = \sqrt{\frac{2}{\omega\mu_0\sigma}}, \tag{4.44}$$

which is generally known as the skin depth. In case δ is small enough, $W(\rho)$ only differs significantly from zero for $\rho \approx a$. In that case, $W(\rho)$ simplifies to

$$W(\rho) = \exp\left[-(a-\rho)/\delta\right], \text{ for } 0 \leq \rho \leq a. \tag{4.45}$$

The current density can then be written as

$$J_z(\mathbf{r}, s) = J_0(z\mathbf{u}_z + a\mathbf{u}_{\rho'}, s)\exp\left[-(a-\rho)/\delta\right], \tag{4.46}$$

where $J_0(z\mathbf{u}_z + a\mathbf{u}_{\rho'}, s)$ denotes the current density that is present on the surface of the wire. We plotted this factor $W(\rho)$ as a function of $0 \leq \rho \leq a$ in Figure 4.2 A. This figure has been plotted in a three-dimensional form to stress that the exponential behavior is observed from every direction normal to the surface of the wire. Note that for visualization purposes, the value for δ has been chosen in such a way here that the behavior of $W(\rho)$ can actually be seen. If we would have chosen a realistic value for δ, which is very small ($\delta << a$), the factor $W(\rho)$ would look like a straight, almost vertical line from $a - \delta$ to a. In case the exponential behavior must be evaluated numerically, the sharp transition at $a - \delta$ however makes it very hard to use straightforward methods. Therefore we approximated W with a Heaviside step function. This step function equals a constant value F if $a - \delta \leq \rho \leq a$ and vanishes elsewhere. Physically this means that we concentrate the current density in a thin, constant layer of a certain skin depth at the surface . This is visualized in Figure 4.2 B. The area $\mathrm{A_w}$ under this window function should equal the area under the actual exponential behavior $\mathrm{A_e}$ to give accurate results for the current. The amplitude of the window function can be varied to arrive at the area under the exponential behavior.

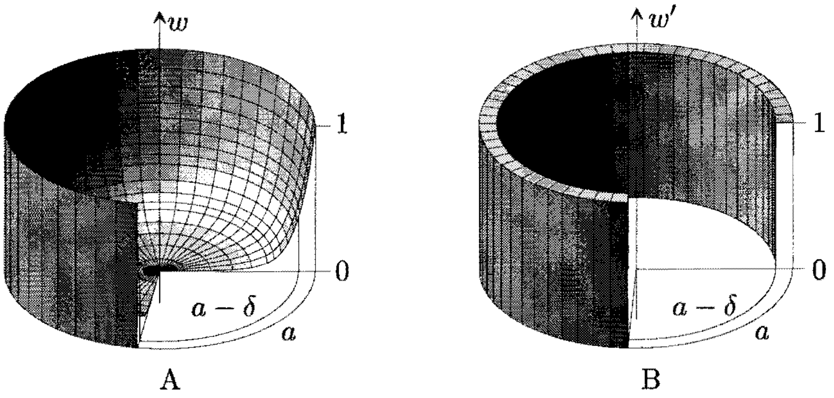

Figure 4.2: *A view of the actual exponential behavior of W (A) and the approximated behavior of W (B).*

Let us introduce the factor F_c, which is defined as

$$F_c = \frac{\mathsf{A}_\mathrm{w}}{\mathsf{A}_\mathrm{e}} = \frac{\displaystyle\int_{a-\delta}^{a} \rho d\rho}{\displaystyle\int_0^a \exp(-(a-\rho)/\delta)\rho d\rho} = \frac{2a-\delta}{2a+2\delta\left[\exp(-a/\delta)-1\right]}, \tag{4.47}$$

where we have taken the amplitude F of the step function to be one. In fact, this factor represents the correction to compensate for the difference in the areas involved. To get insight in the behavior of this factor, we plotted F_c=$\mathsf{A}_\mathrm{w}/\mathsf{A}_\mathrm{e}$ for $\sigma = 5 \cdot 10^7$ S/m, $\sigma = 5 \cdot 10^6$ S/m, $\sigma = 5 \cdot 10^5$ S/m, all with a radius of 0.01m. We also looked at the effect of increasing the radius in Figure 4.3. The approximation becomes almost equal to the actual area under the exponential behavior when the radius is increased. The accuracy with decreasing conductivity however needs to be accounted for by the factor F_c. The inaccuracy is an effect caused by the skin depth. If the conductivity decreases, the skin depth increases and therefore the areas under both functions increases. However, the increase under the step function is larger than under the exponential function for a certain frequency, as is observed from Figure 4.3. Since the total current has to remain the same, we multiply with a factor F_c to arrive at the approximated current.

Now that we have a representation of the current in the approximated case, we can rewrite the vector potential in the scattered field equation Eq. (3.57) for a wire with finite conductivity. The current density to determine the vector potential is taken as

$$J_z(\mathbf{r}', s) = \begin{cases} F_c \dfrac{I_0(z', s)}{\pi[a^2-(a-\delta)^2]}, & \text{for } a-\delta \le \rho' \le a \\ 0, & \text{elsewhere} \end{cases}, \tag{4.48}$$

where the numerator represents the area under the step function. The vector potential from Eq. (3.57) can now be calculated as follows

$$\mathbf{A}_D^e(\mathbf{r}, s) = \frac{1}{\pi[a^2-(a-\delta)^2]} \int_{-L/2}^{L/2} \int_0^{2\pi} \int_{a-\delta}^{a} G(\mathbf{r}-\mathbf{r}', s)\, F_c\, I_0(z', s) \rho' \mathbf{u}_z \, d\rho' d\phi dz', \tag{4.49}$$

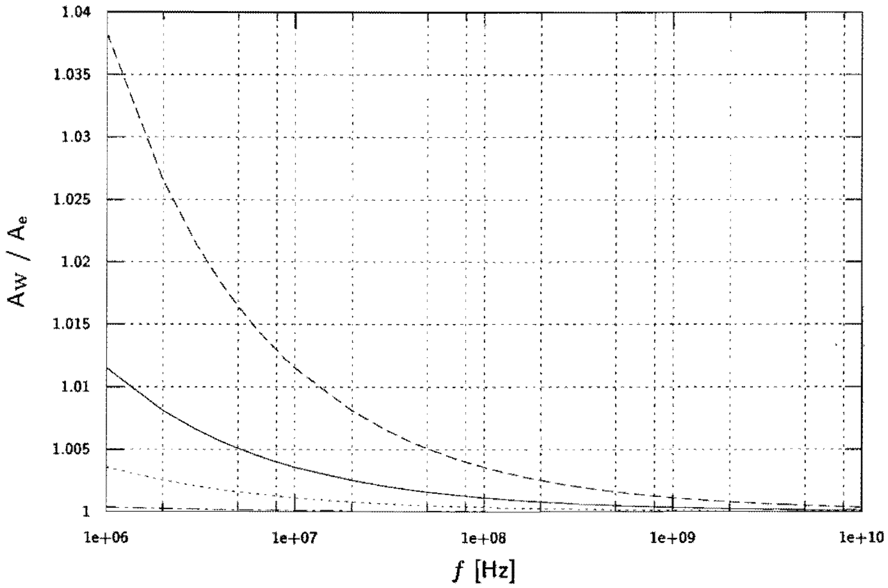

Figure 4.3: *The area under the approximate window-function divided by the area under the actual exponential function versus frequency is plotted here for the configurations:* $\sigma = 5 \cdot 10^7$ *S/m with* $a = 0.01m$ *(dotted line);* $\sigma = 5 \cdot 10^6$ *S/m with* $a = 0.01m$ *(solid line);* $\sigma = 5 \cdot 10^5$ *S/m with* $a = 0.01m$ *(dashed line) and* $\sigma = 5 \cdot 10^7$ *S/m with* $a = 0.1m$ *(dash-dot line).*

Evaluating the integrals in the vector potential with respect to ρ' and ϕ respectively yields

$$\begin{aligned}\mathbf{A}_D^e(z\mathbf{u}_z, s) &= \frac{1}{\pi[a^2-(a-\delta)^2]}\int_{-L/2}^{L/2}\int_0^{2\pi}\left[\frac{\exp\left(-\gamma_0\sqrt{(z-z')^2+(a-\delta)^2}\right)}{4\pi\gamma_0} - \right.\\ &\qquad \left.\frac{\exp\left(-\gamma_0\sqrt{(z-z')^2+a^2}\right)}{4\pi\gamma_0}\right] F_c\, I_0(z', s)\mathbf{u}_z d\phi dz' \\ &= \int_{-L/2}^{L/2} \tilde{G}(z-z', s) I(z', s) dz', \end{aligned} \tag{4.50}$$

where

$$\tilde{G}(z-z', s) = F_c \frac{\exp\left(-\gamma_0\sqrt{(z-z')^2+(a-\delta)^2}\right) - \exp\left(-\gamma_0\sqrt{(z-z')^2+a^2}\right)}{2\pi[a^2-(a-\delta)^2]\gamma_0}. \tag{4.51}$$

4.4 Coupling between two wires

The configuration is given in Figure 4.4. The configuration consists of a passive wire, denoted as wire B and a wire which is excited with a voltage source V_g located in the middle of that wire, denoted as wire A. Since this source is located in a so-called δ-gap, it is also known as a δ-gap source. In this configuration, incident fields from exterior sources are absent. The distance between the wires is denoted as d.

The system of coupled equations is determined by applying the so-called "null-field" condition. Since we look at the current in the z-direction only for both derivations of the scattered field,

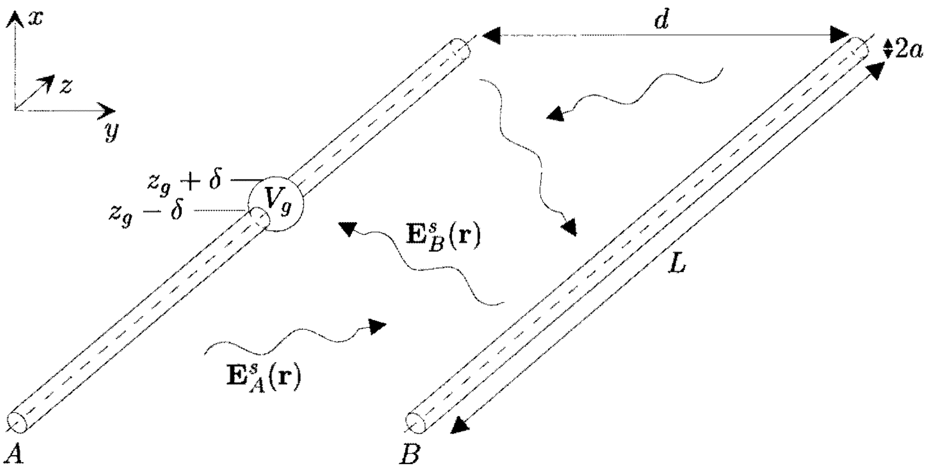

Figure 4.4: *The two-wire problem*

we take the null-field condition $E^s_A(z\mathbf{u}_z, s) + E^i_A(z\mathbf{u}_z, s) + V_g\delta(z - z_g) = 0$. Note that the incident field on wire A is the scattered field from wire B. So the following relations can be constructed

$$E^s_A(z\mathbf{u}_z, s) + E^s_B(z\mathbf{u}_z, s) = -V_g\delta(z - z_g), \tag{4.52}$$

$$E^s_B(z\mathbf{u}_z, s) + E^s_A(z\mathbf{u}_z, s) = 0, \tag{4.53}$$

where z is the observation point on either wire A or wire B, z_g is the location of the δ-gap source.

In the distance term $|\mathbf{r} - \mathbf{r}'|$ occurring in the Green's function, we have to account for the distance d between the wires. If we now concentrate the current on the central axis (see section 4.2) in the computation of the scattered field, the vector potential can be calculated in a straightforward way from a one-dimensional integral over z'. Next we look at Figure 4.5 together with the aid of Pythagoras' theorem to determine $|\mathbf{r}-\mathbf{r}'|$ if the source point is located

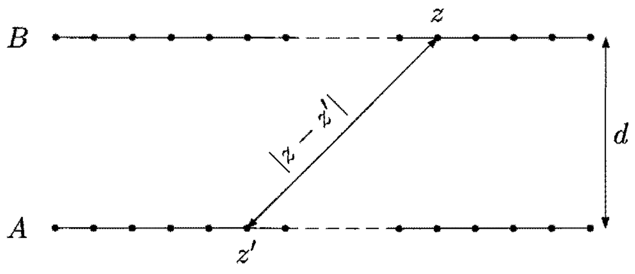

Figure 4.5: *Distance between a source point on wire B and the observation point on wire A.*

on wire B and the observation point is on wire A. The appropriate Green's function now becomes

$$G_{B\to A}(z - z', s) = \frac{\exp(-\gamma_0\sqrt{(z - z')^2 + d^2})}{4\pi\sqrt{(z - z')^2 + d^2}}. \tag{4.54}$$

A similar equation applies when we take the observation point on wire B and the source point on wire A. Now that we have the Green's function from wire A to wire B (and vice versa), we can formulate the vector potentials for both wires. Handling the singularity in the Green's function in the calculation of the vector potential from the wire on which the source point is located has already been described extensively in previous sections.
When the source point is located on wire B and the observation point is located on wire A, the vector potential looks as follows

$$\mathbf{A}_{B\to A}(z,s) = \int_{-L/2}^{L/2} G_{B\to A}(z,s)I_B(z',s)\mathbf{u}_z dz'. \tag{4.55}$$

The scattered field from wire B, incident on wire A, now becomes

$$E_B^s(z,s) = \frac{1}{s\epsilon_0}(\nabla\nabla\cdot - \gamma_0^2)A_{B\to A}(z,s), \tag{4.56}$$

which is expressed in operator notation as

$$E_B^s(z,s) = \mathcal{K}_{B\to A}I_B(z,s). \tag{4.57}$$

Note that we only look at the z-component of $E_B^s(z,s)$. Substituting this and the scattered fields in the null-field conditions (Eqs. (4.52) - (4.53)) yields

$$(\partial_z^2 - \gamma_0^2)\left[\int_{-L_A/2}^{L_A/2} G_{A\to A}(z-z',s)I_A(z',s)dz' \right.$$
$$\left. + \int_{-L_B/2}^{L_B/2} G_{B\to A}(z-z',s)I_B(z',s)dz'\right] = -s\epsilon_0 V_g \delta(z-z_g), \tag{4.58}$$
$$(\partial_z^2 - \gamma_0^2)\left[\int_{-L_A/2}^{L_A/2} G_{A\to B}(z-z',s)I_A(z',s)dz' \right.$$
$$\left. + \int_{-L_B/2}^{L_B/2} G_{B\to B}(z-z',s)I_B(z',s)dz'\right] = 0, \tag{4.59}$$

where L_A and L_B denote the length of wire A and B, respectively. In operator notation we obtain

$$\mathcal{K}_{A\to A}I_A + \mathcal{K}_{B\to A}I_B = -s\epsilon_0 V_g\delta(z-z_g), \tag{4.60}$$
$$\mathcal{K}_{A\to B}I_A + \mathcal{K}_{B\to B}I_B = 0. \tag{4.61}$$

A similar approach can be found in [26]. The latter two equations can be recognized as the matrix operator, so Eqs. (4.60) – (4.61) can also be written as

$$\begin{bmatrix} \mathcal{K}_{A\to A} & \mathcal{K}_{B\to A} \\ \mathcal{K}_{A\to B} & \mathcal{K}_{B\to B} \end{bmatrix} \begin{bmatrix} I_A \\ I_B \end{bmatrix} = \begin{bmatrix} -s\epsilon_0 V_g\delta(z) \\ 0 \end{bmatrix}. \tag{4.62}$$

The operators in the left-hand side of this last equation will be evaluated in Chapter 6, where the operators will be written in a weak form. This weak form can then be solved by the CG-FFT method.

Chapter 5

Coupling between a wire and a dielectric body

In this chapter, we derive the coupling equations that are used to study the mutual coupling between a wire antenna and a three-dimensional dielectric body. The general equations presented in Chapter 3 are solved for the electric field strength.

As a starting point, we have a code available that solves the scattering problem in terms of the electric flux density for a three-dimensional inhomogeneous dielectric object which is illuminated by a plane wave [34]. The electric flux density is being used here rather than the electric field, since the electric flux density normal to the surface is continuous, which is observed from the boundary conditions. The need to have a continuous normal component follows from the discretization procedure and will be discussed later (Section 6.2). The iterative scheme generates the discretized electric flux density as a solution of the integral operation.

The configuration of the problem is given in Figure 5.1. Here we distinguish a bounded,

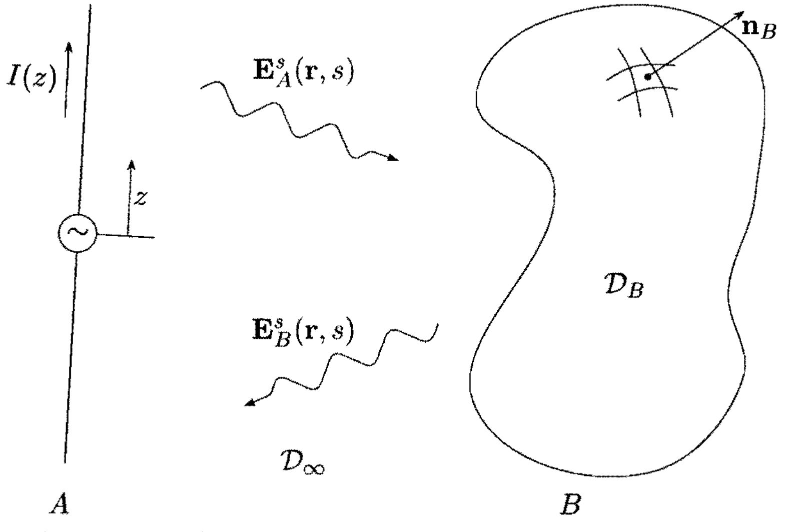

Figure 5.1: *A view of the antenna-body problem*

three-dimensional body with $\mu(\mathbf{r}) = \mu_0$, $\epsilon(\mathbf{r}) \geq 0$, $\sigma(\mathbf{r}) \geq 0$, and a one-dimensional, perfectly conducting wire with a δ-gap excitation in the center.

5.1 Constitutive relations

In this section we define some parameters involving the conversion from the electric field to the electric flux density. The reason for this lies in the fact that a three-dimensional body has different interfaces with strong discontinuities in the dielectric properties of the medium surrounding the object as well as inside the object. These differences in dielectric properties require a correct implementation of the boundary conditions. In the discretization procedure that will be discussed in the next chapter, it is convenient to consider those field quantities as fundamental unknowns whose normal component is continuous at the interface between two adjacent cells. We use the electric flux density to meet this requirement.
The electric flux density is given as

$$\mathbf{D}(\mathbf{r}, s) = \epsilon(\mathbf{r})\mathbf{E}(\mathbf{r}, s). \tag{5.1}$$

The permittivity $\epsilon(\mathbf{r}) = \epsilon_0\epsilon_r(\mathbf{r})$ in Eq. (5.1) depends solely on the dielectric properties of the medium. We distinguish three types of media, which are listed below. It is noted that the first two types occur in "normal" cases, and that the third type is a special case of the second type.

1. **Free space.**
   The electric flux density only differs from the electric field by the factor of ϵ_0. So Eq. (5.1) reduces to
   $$\mathbf{D}(\mathbf{r}, s) = \epsilon_0\mathbf{E}(\mathbf{r}, s). \tag{5.2}$$

2. **Isotropic media.**
   If the permittivity $\epsilon(\mathbf{r})$ and the permeability $\mu(\mathbf{r})(= \mu_0)$ of a body in the neighborhood of some interior point do not behave differently along different directions, the body is called isotropic. The relation between the electric field and the electric flux density is still linear.

3. **Anisotropic media.**
   If the permittivity $\epsilon(\mathbf{r})$ and the permeability $\mu(\mathbf{r})(= \mu_0)$ of a body in the neighborhood of some interior point behave differently along different directions, the medium is called anisotropic. Usually the relation between the electric field and the electric flux density is still linear, but now each of the electric flux density components is written as a linear combination of the electric field components. Eq. (5.1) becomes
   $$\begin{bmatrix} D_x \\ D_y \\ D_z \end{bmatrix} = \epsilon_0 \begin{bmatrix} \epsilon_{11} & \epsilon_{12} & \epsilon_{13} \\ \epsilon_{21} & \epsilon_{22} & \epsilon_{23} \\ \epsilon_{31} & \epsilon_{32} & \epsilon_{33} \end{bmatrix} \begin{bmatrix} E_x \\ E_y \\ E_z \end{bmatrix}, \tag{5.3}$$
   where the quantity $\epsilon(\mathbf{r})$ in Eq. (5.1) is a tensor of rank two. Note that the quantity $\epsilon(\mathbf{r})$ can depend on the frequency (see Eq. (5.5)).

Since we do not consider anisotropic media in our problem, we consider materials of type two only.

Next we rewrite the current density from Eq. (3.57) as

$$\mathbf{J}^e_D(\mathbf{r},s) = s\epsilon_0\tilde{\epsilon}(\mathbf{r},s)\mathbf{E}(\mathbf{r},s) - s\epsilon_0\mathbf{E}(\mathbf{r},s), \tag{5.4}$$

where

$$\tilde{\epsilon}(\mathbf{r},s) = \epsilon_r(\mathbf{r}) + \frac{\sigma(\mathbf{r})}{s\epsilon_0}, \tag{5.5}$$

is denoted as the complex relative permittivity. By using the definition of the electric flux density, Eq. (5.4) can be rewritten as

$$\mathbf{J}^e_D(\mathbf{r},s) = s\chi(\mathbf{r},s)\mathbf{D}(\mathbf{r},s), \tag{5.6}$$

where

$$\chi(\mathbf{r},s) = \frac{\tilde{\epsilon}(\mathbf{r},s) - 1}{\epsilon_r(\mathbf{r})}. \tag{5.7}$$

Note that this definition differs from the conventional notation of the dielectric susceptibility. Now that the relevant parameters for conversion of the field quantities into flux densities have been defined, we can formulate the integral equations.

5.2 Integral equations

In order to rewrite the total field $\mathbf{E} = \mathbf{E}^i + \mathbf{E}^s$ of the body, we need an expression for the vector potential in the scattered field Eq. (3.57) in terms of the electric flux density. The vector potential becomes

$$\mathbf{A}^e_D(\mathbf{r},s) = \int_{\mathbf{r}'\in\mathcal{D}_B} G(\mathbf{r}-\mathbf{r}',s)\; s\chi(\mathbf{r})\; \mathbf{D}(\mathbf{r}',s)d\mathbf{r}'. \tag{5.8}$$

By using this definition, the total electric field of the body follows from

$$\mathbf{E}(\mathbf{r}) = \frac{1}{\epsilon(\mathbf{r})}\mathbf{D}(\mathbf{r},s) = \mathbf{E}^i(\mathbf{r},s) + (s\epsilon_0)^{-1}\left(\nabla\nabla\cdot - \gamma_0^2\right)\mathbf{A}^e_D(\mathbf{r},s), \tag{5.9}$$

where the total electric field itself is written in terms of the electric flux density. In operator notation, Eq. (5.9) is of the form

$$\mathbf{E}^i(\mathbf{r},s) + \left[\mathcal{K}_{B\to B} - \frac{1}{\epsilon(\mathbf{r})}I\right]\mathbf{D}(\mathbf{r},s) = \mathbf{0}, \tag{5.10}$$

where I again is the identity matrix.

5.3 Coupling between a dielectric body and a wire antenna

To arrive at the desired form for the general configuration, we only need to replace the incident electric field in Eq. (5.9) with the scattered field from a wire antenna, and substitute the corresponding scattered field as incident field in the thin-wire integral equation Eq. (4.58). The equations for the field quantity on the central axis of the wire and inside the dielectric body become

$$(s\epsilon_0)^{-1}\Bigg[\mathbf{u}_z\cdot(\nabla\nabla\cdot-\gamma_0^2)\int_{\mathbf{r}'\in\mathcal{D}_B}G_{B\to A}(z\mathbf{u}_z-\mathbf{r}',s)s\chi(\mathbf{r}')\mathbf{D}_B(\mathbf{r}',s)d\mathbf{r}'\;+$$
$$(\partial_z^2-\gamma_0^2)\int_{-L/2}^{L/2}G_{A\to A}(z\mathbf{u}_z-z',s)I_A(z',s)dz'\Bigg]=-V_g\delta(z),\;\text{for}\;-L/2<z<L/2,\tag{5.11}$$

$$(s\epsilon_0)^{-1}\Bigg[(\nabla\nabla\cdot-\gamma_0^2)\int_{\mathbf{r}'\in\mathcal{D}_B}G_{B\to B}(\mathbf{r}-\mathbf{r}',s)s\chi(\mathbf{r}')\mathbf{D}_B(\mathbf{r}',s)d\mathbf{r}'+$$
$$(\partial_z^2-\gamma_0^2)\int_{-L/2}^{L/2}\frac{1}{s}G_{A\to B}(\mathbf{r}-z'\mathbf{u}_z,s)I_A(z',s)dz'\Bigg]=\frac{\mathbf{D}_B(\mathbf{r},s)}{\epsilon(\mathbf{r})},\;\text{for}\;\mathbf{r}\in\mathcal{D}_B.\tag{5.12}$$

In operator notation Eqs. (5.11) – (5.12) become

$$\begin{bmatrix}\mathcal{K}_{A\to A} & \mathcal{K}_{B\to A}\\ \mathcal{K}_{A\to B} & \mathcal{K}_{B\to B}-\frac{1}{\epsilon(\mathbf{r})}I\end{bmatrix}\begin{bmatrix}I_A\\ \mathbf{D}_B\end{bmatrix}=\begin{bmatrix}-V_g\\ \mathbf{0}\end{bmatrix},\tag{5.13}$$

where each of the lines refers to observation in the relevant domain as specified above. The $\mathcal{K}_{A\to B}$ operator in this matrix form contains a Green's function as given in Eq. (3.27). The distance between a source point and an observation point is depicted in Figure 5.2. Here, we have chosen to place the center of the wire at a distance d from the center of the three-dimensional body B. The distance follows from using Pythagoras' theorem, where the distance d has to be added to the y-coordinate of the observation point for this configuration. This leaves us with

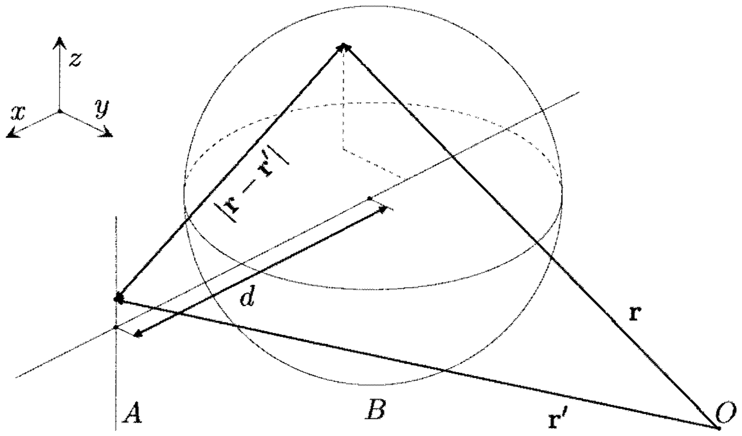

Figure 5.2: *Distance d between a source point $\mathbf{r}'$ on the wire (A) and an observation point $\mathbf{r}$ inside the dielectric body (B).*

$$G_{A\to B}(\mathbf{r},z',s)=\frac{\exp\left(-\gamma_0|\mathbf{r}-\mathbf{r}'|\right)}{4\pi|\mathbf{r}-\mathbf{r}'|}.\tag{5.14}$$

With $\mathbf{r}=x\mathbf{u}_x+y\mathbf{u}_y+z\mathbf{u}_z$ and $\mathbf{r}'=d\mathbf{u}_x+z'\mathbf{u}_z$ Eq. (5.14) becomes

$$G_{A\to B}(\mathbf{r},z',s)=\frac{\exp\left(-\gamma_0\sqrt{(x-d)^2+y^2+(z-z')^2}\right)}{4\pi\sqrt{(x-d)^2+y^2+(z-z')^2}}.\tag{5.15}$$

The matrix-operator described here will be solved numerically for some practical coupling problems using the WCG-FFT method. But first the equations have to be weakened and discretized in a proper manner. This will be discussed in the next chapter.

Chapter 6

Numerical implementation

In this chapter, we discuss the discretization procedure for the integral equations that are described in the previous chapters. We particularly discuss the discretization of the integral equations of the two-wire problem. The extension to the discretization of the antenna-body problem follows by analogy. Also the choice of rooftop functions as testing and expansion functions in the three-dimensional case will be explained.

As a next step, we present the method of solution for the currents on both wires. In this procedure we use the conjugate-gradient FFT method to solve the weak form of the discretized integral equations. The discrete Fourier transformation and the appropriate operators needed in the method of solution for the two-wire problem are discussed as well.

The integral relations concerning the body-antenna problem will not be discussed here since the discretization process of the two-wire problem provides sufficient insight in obtaining discretized integral relations which can be solved with the weak conjugate-gradient - FFT method. However, more information about the discretization procedure in the three-dimensional case can be found in literature [34], [36].

6.1 Discretization procedure

As a point of departure we use Eqs. (4.58) – (4.59):

$$(\partial_z^2 - \gamma_0^2)\left[\int_{-L_A/2}^{L_A/2} G_{A\to A}(z-z',s)I_A(z',s)dz' + \int_{-L_B/2}^{L_B/2} G_{B\to A}(z-z',s)I_B(z',s)dz'\right] = -s\epsilon_0 V_g \delta(z-z_g), \text{ for } -L_A/2 < z < L_A/2, \quad (6.1)$$

$$(\partial_z^2 - \gamma_0^2)\left[\int_{-L_A/2}^{L_A/2} G_{A\to B}(z-z',s)I_A(z',s)dz' + \int_{-L_B/2}^{L_B/2} G_{B\to B}(z-z',s)I_B(z',s)dz'\right] = 0, \text{ for } L_B/2 < z < L_B/2. \quad (6.2)$$

These relations are rewritten as

$$(\partial_z^2 - \gamma_0^2)\left[A_{A\to A}(z,s) + A_{B\to A}(z,s)\right] = -s\epsilon_0 V_g \delta(z - z_g), \text{ for } -L_A/2 < z < L_A/2 \tag{6.3}$$
$$(\partial_z^2 - \gamma_0^2)\left[A_{A\to B}(z,s) + A_{B\to B}(z,s)\right] = 0, \text{ for } L_B/2 < z < L_B/2. \tag{6.4}$$

where $A_{\{A\to A, A\to B, B\to A, B\to B\}}(z,s)$ denote the vector potentials as described earlier and $V_g\delta(z-z_g)$ represents a delta-gap source in the center of wire A.

First we divide the domain of integration into $M_{A,B} - 1$ subdomains. This leaves us with $M_{A,B}$ sample points which are located in the center of each subdomain (the position of the sample points will be discussed further on). These subdomains provide a mesh with grid size $\Delta z = L_{A,B}/(M_{A,B} - 1)$, where the subscripts $_{A,B}$ pertain to wire A and wire B, respectively. Note that $M_{A,B}$ should be large enough to meet the requirement that the current may be approximated by a constant value in each subdomain.

Second we multiply this strong form with a scalar testing function $\psi_n(z)$, with $n \in \{1, ..., M_{A,B}\}$, and integrate the result over the wire support $\mathcal{D}_{A,B}$. The latter two integral relations become

$$\gamma_0^2 \int_{z\in\mathcal{D}_A} \psi_n(z)\left[A_{A\to A}(z,s) + A_{B\to A}(z,s)\right] dz - \int_{z\in\mathcal{D}_A} \psi_n(z)\partial_z^2 \left[A_{A\to A}(z,s) + A_{B\to A}(z,s)\right] dz = s\epsilon_0 \psi_n(z_g) V_g, \tag{6.5}$$

$$\gamma_0^2 \int_{z\in\mathcal{D}_B} \psi_n(z)\left[A_{A\to B}(z,s) + A_{B\to B}(z,s)\right] dz - \int_{z\in\mathcal{D}_B} \psi_n(z)\partial_z^2 \left[A_{A\to B}(z,s) + A_{B\to B}(z,s)\right] dz = 0. \tag{6.6}$$

With the aid of the product rule for differentiation, integration by parts and the assumption that $\psi_n(z)$ vanishes for $z \in \partial\mathcal{D}\ \forall_{n=1,\ldots,M_{A,B}}$, Eqs. (6.5) – (6.6) can be rewritten as

$$\gamma_0^2 \int_{z\in\mathcal{D}_A} \psi_n(z)\left[A_{A\to A}(z,s) + A_{B\to A}(z,s)\right] dz - \int_{z\in\mathcal{D}_A} \partial_z\psi_n(z)\partial_z \left[A_{A\to A}(z,s)dz + A_{B\to A}(z,s)\right] dz = s\epsilon_0 \psi_n(z_g) V_g, \tag{6.7}$$

$$\gamma_0^2 \int_{z\in\mathcal{D}_B} \psi_n(z)\left[A_{A\to B}(z,s) + A_{B\to B}(z,s)\right] dz - \int_{z\in\mathcal{D}_B} \partial_z\psi_n(z)\partial_z \left[A_{A\to B}(z,s) + A_{B\to B}(z,s)\right] dz = 0 \tag{6.8}$$

Before we can take the last step in the discretization procedure we need to define the position of the sample points on the wire. The position of the $m_{A,B}^{\text{th}}$ sample along the wire axis is given by

$$z_{m_{A,B}} = (m_{A,B} - 1)\,\Delta z - L_{A,B}/2, \quad m_{A,B} = 1, ..., M_{A,B}, \tag{6.9}$$

which is depicted in Figure 6.1. With this choice of subdomain distribution along the wire, each sampling point is located at the center of a subdomain.

Finally, the electric vector potentials and the field originating from the delta-gap source are expanded in a sequence of subdomain expansion functions $\phi_m(z)$, with $m = 1, ..., M_{A,B}$. These

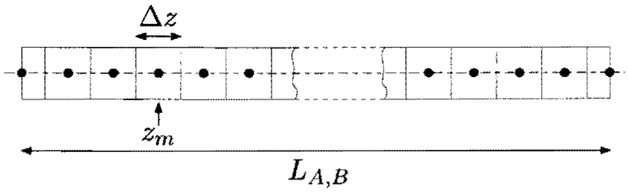

Figure 6.1: *The discretization grid with mesh size* Δz*.*

expansion functions are chosen to be identical to the testing functions, hence $\phi_m(z) = \psi_m(z)$, which is known as the Galerkin procedure. This leads to

$$A_{\{A\to A,B\to A\}}(z_m) = \sum_{m=1}^{M_A-1} A_{\{A\to A,B\to A\},m}\psi_m(z), \quad z \in \mathcal{D}_A, \tag{6.10}$$

$$A_{\{A\to B,B\to B\}}(z_m) = \sum_{m=1}^{M_B-1} A_{\{A\to B,B\to B\},m}\psi_m(z), \quad z \in \mathcal{D}_B. \tag{6.11}$$

Substituting this result in Eq. (6.7) and interchanging the order of summation and integration leaves us with

$$\begin{aligned}
&\sum_{n=1}^{M_A-1} A_{A\to A,n}\left[\int_{z\in\mathcal{D}_A} \partial_z\psi_m(z)\partial_z\psi_n(z)dz - \gamma_0^2\int_{z\in\mathcal{D}_A}\psi_m(z)\psi_n(z)dz\right] + \\
&\sum_{n=1}^{M_A-1} A_{B\to A,n}\left[\int_{z\in\mathcal{D}_A} \partial_z\psi_m(z)\partial_z\psi_n(z)dz - \gamma_0^2\int_{z\in\mathcal{D}_A}\psi_m(z)\psi_n(z)dz\right] = \\
&\qquad V_g\delta_{z_m,z_g}, \quad m = 1,...,M_A,
\end{aligned} \tag{6.12}$$

$$\begin{aligned}
&\sum_{n=1}^{M_B-1} A_{A\to B,n}\left[\int_{z\in\mathcal{D}_B} \partial_z\psi_m(z)\partial_z\psi_n(z)dz - \gamma_0^2\int_{z\in\mathcal{D}_B}\psi_m(z)\psi_n(z)dz\right] + \\
&\sum_{n=1}^{M_B-1} A_{B\to B,n}\left[\int_{z\in\mathcal{D}_B} \partial_z\psi_m(z)\partial_z\psi_n(z)dz - \gamma_0^2\int_{z\in\mathcal{D}_B}\psi_m(z)\psi_n(z)dz\right] = 0, \\
&\qquad m = 1,...,M_B,
\end{aligned} \tag{6.13}$$

in which δ_{z_m,z_g} denotes the Kronecker symbol, which is defined as

$$\delta_{m,n} = \begin{cases} 1 & \text{if } m = n, \\ 0 & \text{if } m \neq n. \end{cases} \tag{6.14}$$

For the sake of convenience, we rewrite Eqs. (6.12) - 6.13 as

$$\sum_{n=1}^{M_A-1} \left[A_{A\to A,n} + A_{B\to A,n}\right]\left[w_{m;n} - \gamma_0^2 v_{m;n}\right] = V_g\delta_{z_m,z_g}, \; m = 1,...,M_A, \tag{6.15}$$

$$\sum_{n=1}^{M_B-1} \left[A_{A\to B,n} + A_{B\to B,n}\right]\left[w_{m;n} - \gamma_0^2 v_{m;n}\right] = 0, \; m = 1,...,M_B \tag{6.16}$$

where

$$v_{m;n} = \int_{z\in\{\mathcal{D}_A,\mathcal{D}_B\}} \psi_m(z)\psi_n(z)dz\,, \tag{6.17}$$

$$w_{m;n} = \int_{z\in\{\mathcal{D}_A,\mathcal{D}_B\}} \partial_z\psi_m(z)\;\partial_z\psi_n(z)dz\,. \tag{6.18}$$

We now have a system of equations that can be solved numerically.

6.2 Testing and expansion functions

In this section the choice of a particular kind of testing and expansion function is justified. Before writing down the possible choices, we give a set of requirements that are valid for an object to be discretized.
For a correct implementation of the discretized integral relation, the expansion functions should meet the following requirements:

- the partial derivative $\partial_z \psi_m(z)$ exists and is piecewise constant for $z \in \mathcal{D}$; it should not contain δ-functions;
- $\psi_m(z)$ vanishes for $z \in \partial\mathcal{D}$;
- $\psi_m(z)$ is chosen such that the sets of expansion coefficients $A_{\{\frac{A}{B}\to\frac{A}{B}\},m}$ and V_m are easily obtained from $A_{\{\frac{A}{B}\to\frac{A}{B}\}}(z)$ and V_g, by using Eqs. (6.10) – (6.11).

With these requirements and some knowledge about the behavior of the quantities to be solved from the discretized relation, a suitable choice for the testing and expansion functions can be made. Note that the second requirement also applies to the field component under study. Because the electric flux density satisfies the requirement that its component normal to the interfaces inside an object is continuous, we take the electric flux density instead of the electric field in a three-dimensional body. In this case the testing and expansion functions are vectorial quantities and the normal component.
In testing and expanding the components of an integral relation in a subdomain, we examine if the following, most commonly used, functions (see Figure 6.2) meet all our requirements. In

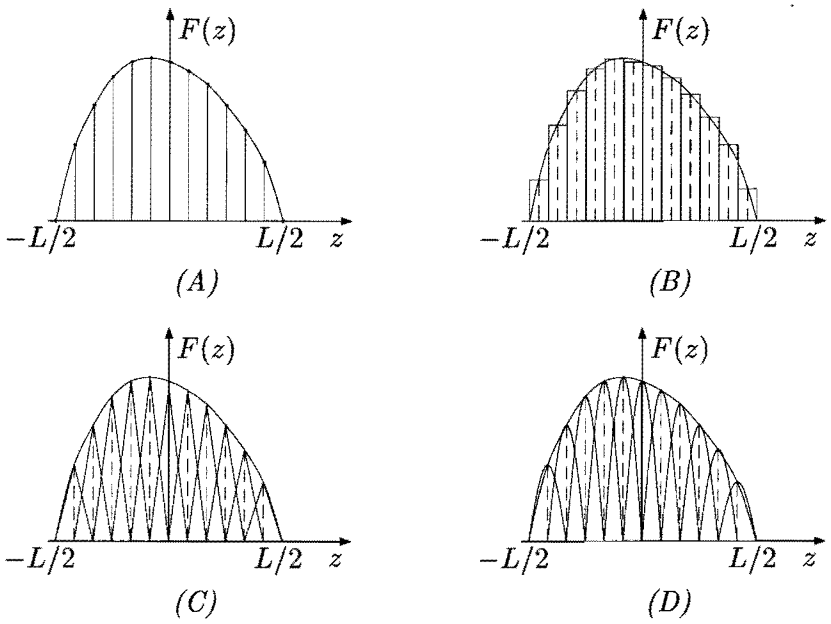

Figure 6.2: *An arbitrary function $F(z)$ approximated by delta (A); pulse (B); triangle (C) and trigonometric functions (D).*

the specification of these possible testing and expansion functions we use $\psi_k(z) = \psi_0(z - z_k)$.

1. Delta functions

$$\psi_0(z) = \delta(z), \quad z \in (-L/2, L/2). \tag{6.19}$$

2. Pulse functions

$$\psi_0(z) = \begin{cases} 1 & -\frac{\Delta z}{2} < z < \frac{\Delta z}{2}, \\ \frac{1}{2} & |z| = \frac{\Delta z}{2}, \\ 0 & \text{elsewhere.} \end{cases} \tag{6.20}$$

3. Triangle functions

$$\psi_0(z) = \begin{cases} 1 - \frac{|z|}{\Delta z} & -\Delta z \leq z \leq \Delta z, \\ 0 & \text{elsewhere.} \end{cases} \tag{6.21}$$

4. Trigonometric functions

$$\psi_0(z) = \begin{cases} \cos\left(\frac{\pi |z|}{2\Delta z}\right) & -\Delta z \leq z \leq \Delta z, \\ 0 & \text{elsewhere.} \end{cases} \tag{6.22}$$

We already have obtained a set of requirements with which the testing and expansion functions must comply, as well as a set of functions from which we can choose.
The functions that meet all requirements are the triangle and trigonometric functions. The first derivative of the triangle function is a constant value, whereas the first derivative of the trigonometric function is again a trigonometric function. From the set of rules, it follows that the derivative has to exist, hence it is sufficient to use the triangle function as testing and expansion function for the current distribution in the wire.
In a two or three-dimensional body, the current (density) distribution is no longer limited to a single direction. To meet all requirements in this case, we use rooftop functions as testing and expansion functions. A rooftop function is constructed from a triangle function and one or two pulse functions, respectively. More information about the rooftop function can be found in the literature [9], [34].

6.3 The discretized relation

With the particular choice of triangle functions as testing and expansion functions, we can determine Eqs. (6.17) – (6.18) analytically. This leads to

$$v_{m;n} = \frac{\Delta z}{6}\left[\delta_{n,m-1} + 4\delta_{n,m} + \delta_{n,m+1}\right], \tag{6.23}$$

$$w_{m;n} = \frac{1}{\Delta z}\left[-\delta_{n,m-1} + 2\delta_{n,m} - \delta_{n,m+1}\right], \tag{6.24}$$

in which $\delta_{n,m}$ is again the kronecker delta. Using Eqs. (6.23) – (6.24) we obtain for Eq. (6.15)

$$\tilde{v}_n = \frac{1}{s\epsilon_0} \sum_{k=1}^{3} \left[d_k A_{A\to A,n+k-2} + d_k A_{B\to A,n+k-2} \right], \tag{6.25}$$

where

$$d_k = \gamma_0^2 v_{2;k} + w_{2,k}, \tag{6.26}$$

and where the values for $\tilde{v}_n$ is defined as

$$\tilde{v}_n = \frac{\Delta z}{6} \left[V_{n-1} + 4V_n + V_{n+1} \right]. \tag{6.27}$$

Now the integral relation pertaining to wire A has been discretized. A similar relation holds for wire B.

The discretized relation of the three-dimensional body proceeds along similar lines as the ones above. For a detailed description of the discretized-body integral equations, we refer to Zwamborn [34].

6.3.1 The weak form of the discretized relation

In this section we describe the formulation of the weak form of the discretized relation Eq. (6.25). The objective of weakening a function consistent with the discretized relation is to circumvent singular behavior that complicates numerical computation. In this section, we arrive at a weakened form of the Green's function. To demonstrate how this is done in general, we use the Green's function of a three-dimensional body and a wire antenna.

The weak form of the Green's function of a three-dimensional body

We assume a uniform mesh size Δx in all directions. The strong form of the Green's function is weakened by taking the spherical mean. Let us define the spherical mean $[G](\mathbf{r})$ of $G(\mathbf{r})$ as

$$[G](\mathbf{r}, s) = \frac{\displaystyle\int_{|\mathbf{r}''|<\Delta x/2} G(\mathbf{r}+\mathbf{r}'', s) d\mathbf{r}''}{\displaystyle\int_{|\mathbf{r}''|<\Delta x/2} d\mathbf{r}''}, \tag{6.28}$$

where $\mathbf{r}$ is a discretized point here in the domain of integration. The choice of the radius of the region over which we take the average is more or less arbitrary. To obtain consistency with the mesh size we take the largest spherical mean without crossing the integration domain that corresponds to a neighboring discretized point $\mathbf{r} \pm \Delta x \mathbf{u}_{\{x,y,x\}}$.

The weak form of the Green's function of a wire antenna

We assume a uniform mesh size Δx in the z-direction. The strong form of the Green's function is weakened by taking the cylindrical mean. The cylindrical mean is defined as

$$[G](\mathbf{r}, s) = \frac{\displaystyle\int_{z_m-\Delta z/2}^{z_m+\Delta z/2} \int_0^{2\pi} \int_0^a G(\mathbf{r}+\mathbf{r}'', s) \rho'' d\rho'' d\phi'' dz''}{\displaystyle\int_{z_m-\Delta z/2}^{z_m+\Delta z/2} \int_0^{2\pi} \int_0^a \rho'' d\rho'' d\phi'' dz''}, \tag{6.29}$$

where **r** is again a discretized point here in the domain of integration.

The weakened discretized integral relation

Now that the weak form of the Green's function for a wire antenna has been defined, we can give the weak form of Eq. (6.25)

$$\tilde{v}_n = \frac{1}{s\epsilon_0} \sum_{k=1}^{3} \left[d_k \left[A\right]_{A\to A,n+k-2} + d_k \left[A\right]_{B\to A,n+k-2} \right], \; n = 1, ..., M_A, \tag{6.30}$$

where $[A]$ denotes the cylindrical mean of the vector potential A. Note that applying the cylindrical mean of the Green's function in the convolution integral is the same as applying the cylindrical mean on the strong form of the vector potential. This is easily understood by interchanging the order of integration. The weakened form of v_n is written as

$$v_n = \frac{\Delta z}{6} \left[[V]_{n-1} + 4\,[V]_n + [V]_{n+1} \right]. \tag{6.31}$$

The discretized integral relation has now been written in a weak form. Now we only have to evaluate the field quantities. This is done in the next section.

6.3.2 The weak form of the vector potential

In this section the weak representations of the field quantities are being presented. This is done by taking the cylindrical mean and determining the integrals involved analytically.
Let us recall the Green's function in the vector potential of a wire from Chapter 4

$$\tilde{G}(z_m, s) = F_c \, \frac{\exp\left(-\gamma_0 \sqrt{(z_m)^2 + (a-\delta)^2}\right) - \exp\left(-\gamma_0 \sqrt{(z_m)^2 + a^2}\right)}{2\pi[a^2 - (a-\delta)^2]\gamma_0}. \tag{6.32}$$

Note that the Green's function mentioned here has been partially weakened already in the integral over the cross section of the wire. To clarify this remark, let us recall the cylindrical mean from the previous section. Here the integrals with respect to ρ'' and ϕ'' have already been evaluated in the determination of the integral equation pertaining to a wire antenna. This left us with the Green's function as defined in Eq. (4.51). In this case, determination of the integrals in the weakened Green's function leaves us with

$$\left[\tilde{G}\right](z_m, s) = \frac{1}{\Delta z} \int_{z_m - \Delta x/2}^{z_m + \Delta x/2} \tilde{G}(z_m + z'')dz''. \tag{6.33}$$

The convolution integral in the vector potential will be calculated with the aid of the discrete convolution theorem, which will be described in the next section. The Green's function $G_{\{A\to B, B\to A\}}$ from Eq. (4.54) is evaluated at the sample points. This means that in the discretized form of this equation, we simply substitute the values for z_m and the discrete values of the source points.

6.3.3 The one-dimensional discrete Fourier transformation

We define the discrete Fourier transform (DFT) of a given sequence f_m, with $m = 0, ..., N-1$, as

$$\check{f}_n = \sum_{m=0}^{N-1} f_m \exp\left(\frac{2\pi i n m}{N}\right), \tag{6.34}$$

where $n = 0, ..., N-1$. The DFT also has an inverse counterpart DFT^{-1}, which is defined as

$$f_m = \frac{1}{N}\sum_{n=0}^{N-1} \check{f}_n \exp\left(-\frac{2\pi i m n}{N}\right). \tag{6.35}$$

Since $\exp\left[2\pi i(m+nN)/N\right] = \exp\left(2\pi i m/N\right)\exp\left(2\pi i n N/N\right) = \exp\left(2\pi i m\right)$, the DFT quantities $\check{f}_n$ and f_m are both periodic with periodicity N, so the DFT-quantities satisfy the relations

$$\check{f}_{n+mN} = \check{f}_n, \tag{6.36}$$

$$f_{m+nN} = f_m. \tag{6.37}$$

A property of the DFT that we are particularly interested in, is the discrete convolution theorem. This theorem is defined as

$$\sum_{m'=0}^{N-1} f_{m-m'}g_{m'} = \mathrm{TR}_N\left[\mathrm{DFT}_{2N}^{-1}\left\{\mathrm{DFT}_{2N}\left\{f_{m'}\right\}\mathrm{DFT}_{2N}\left[g_{m'}\right\}\right\}\right], \tag{6.38}$$

where g is a symetrical sequence and f is a causal sequence (see Figure 6.3). The DFT can be easily evaluated by using an FFT algorithm. Note that the FFT is most efficiently if N is a power of 2. If the problem contains two bodies, which is the case here, we should choose N twice the number of samples for each object occurring in a convolutional integral.

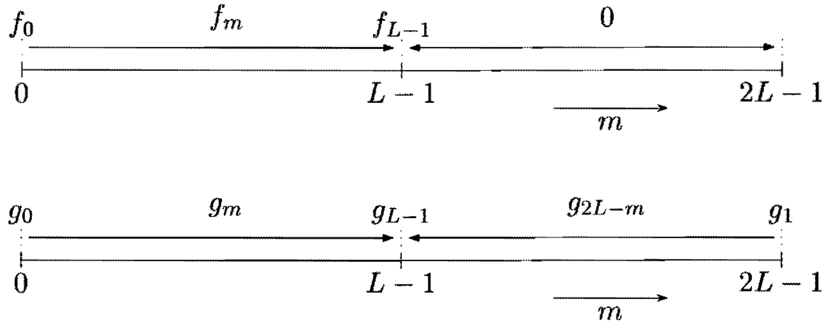

Figure 6.3: *Defenition of the sequences for the discrete convolution theorem.*

6.4 The conjugate-gradient method

Since we only used the standard version of the conjugate-gradient method, we do not explain this method in full detail. Extensive information about the conjugate-gradient method can be found in the literature, see e.g. [9], [34].

The conjugate-gradient scheme is an efficient iterative scheme to solve a system of equations of the form

$$Lu = v, \tag{6.39}$$

where u represents the current on the wires, v denotes the delta-gap source and L denotes a linear operator. Note that the v is a known set of variables and u is the set of variables to be solved. Almost all iterative schemes for this kind of equation have in common that an appropriately chosen error norm is to be minimized. The conjugate-gradient method is based on minimizing the residual error after each iterationstep. Thus we can solve the set of equations to a certain, given degree of accuracy.

Let us define the inner product of two arbitrary sets of variables f and g over the domain of the operator as

$$< f, g >= \int_{\mathbf{r}\in\mathcal{D}} f(\mathbf{r})g^*(\mathbf{r})d\mathbf{r}, \tag{6.40}$$

where g^* is the complex conjugate of g. Next we define the norm of a set of variables f as

$$||f|| = \sqrt{< f, f >}. \tag{6.41}$$

The last quantity needed in the conjugate-gradient method is the adjoint operator, which is defined as the operator that satisfies

$$< Lf, g >=< f, L^\dagger g >, \tag{6.42}$$

for any suitable set of variables f and g.

If we now write the approximation of u in the n^{th} iteration as $u^{(n)}$, then the residual error $r^{(n)}$ is defined as

$$r^{(n)} = v - Lu^{(n)}. \tag{6.43}$$

Now that all necessary building blocks for the conjugate-gradient scheme have been defined, we present the iterative scheme. We choose zero as initial estimate, so $u^{(0)} = 0$. Consequently the residual error $r^{(0)} = v$ for $n = 0$. The iterative scheme for $n = 1$ then looks as

$$\xi^{(1)} = L^\dagger r^{(0)}, \tag{6.44}$$

$$\alpha^{(1)} = \frac{||L^\dagger r^{(0)}||^2}{||L\xi^{(1)}||^2}, \tag{6.45}$$

$$u^{(1)} = \alpha^{(1)}\xi^{(1)}, \tag{6.46}$$

$$r^{(1)} = r^{(0)} - \alpha^{(1)}L\xi^{(1)}. \tag{6.47}$$

The steps for $n = 2, \ldots$ are of the form

$$\beta^{(n)} = \frac{||L^\dagger r^{(n-1)}||^2}{||L^\dagger r^{(n-2)}||^2}, \tag{6.48}$$

$$\xi^{(n)} = L^\dagger r^{(n-1)} + \beta^{(n)}\xi^{(n-1)}, \tag{6.49}$$

$$\alpha^{(n)} = \frac{||L^\dagger r^{(n-1)}||^2}{||L\xi^{(n)}||^2}, \tag{6.50}$$

$$u^{(n)} = u^{(n-1)} + \alpha^{(n)}\xi^{(n)}, \tag{6.51}$$

$$r^{(n)} = r^{(n-1)} - \alpha^{(n)}L\xi^{(n)}. \tag{6.52}$$

Now that the iterative procedure is known, we need to define the operators L and $L^\dagger$ following from the vector potentials in the integral relations.

6.5 Determination of the operators L and $L^\dagger$

In this section we derive the linear operator and his adjoint. As a point of departure we use Eq. (6.25), which is written as

$$v = Lu. \tag{6.53}$$

The convolution in the vector potentials can be approximated using the discrete Fourier transform (DFT) as follows

$$A_{A\to A} = \mathrm{TR}_N\left[\mathrm{DFT}_{2N}^{-1}\left\{\mathrm{DFT}_{2N}\left\{G_{A\to A}\right\}\mathrm{DFT}_{2N}\left\{I_A\right\}\right\}\right], \tag{6.54}$$

$$A_{B\to A} = \mathrm{TR}_N\left[\mathrm{DFT}_{2N}^{-1}\left\{\mathrm{DFT}_{2N}\left\{G_{B\to A}\right\}\mathrm{DFT}_{2N}\left\{I_B\right\}\right\}\right], \tag{6.55}$$

$$A_{A\to B} = \mathrm{TR}_N\left[\mathrm{DFT}_{2N}^{-1}\left\{\mathrm{DFT}_{2N}\left\{G_{A\to B}\right\}\mathrm{DFT}_{2N}\left\{I_A\right\}\right\}\right], \tag{6.56}$$

$$A_{B\to B} = \mathrm{TR}_N\left[\mathrm{DFT}_{2N}^{-1}\left\{\mathrm{DFT}_{2N}\left\{G_{B\to B}\right\}\mathrm{DFT}_{2N}\left\{I_B\right\}\right\}\right]. \tag{6.57}$$

To avoid aliasing in the convolution between G and I, the number of points for the FFT should be taken at least twice the value of the sampling rate, so $N \geq 2M_{A,B}$. The adjoint operator $L^\dagger$ in the discretized integral relation (6.25) is related to the operator L as

$$\langle Lu, r\rangle = \left\langle u, L^\dagger r\right\rangle, \tag{6.58}$$

in which r is an arbitrary discrete function. Substitution of Eq. (6.53) in this latter equation leads to

$$\xi = L^\dagger r \tag{6.59}$$

as follows

$$\xi_{m_A} = \sum_{k=1}^{3}\left[\hat{d}_k^* Q_{A\to A,m+k-2} + \hat{d}_k^* Q_{B\to A,m+k-2}\right], \tag{6.60}$$

$$\xi_{m_B} = \sum_{k=1}^{3}\left[\hat{d}_k^* Q_{A\to B,m+k-2} + \hat{d}_k^* Q_{B\to B,m+k-2}\right], \tag{6.61}$$

where

$$Q_{A\to A} = \mathrm{TR}_N\left[\mathrm{DFT}_{2N}^{-1}\left\{\mathrm{DFT}_{2N}\left\{G^*_{A\to A}\right\}\mathrm{DFT}_{2N}\left\{I_A{}^*\right\}\right\}\right], \tag{6.62}$$

$$Q_{B\to A} = \mathrm{TR}_N\left[\mathrm{DFT}_{2N}^{-1}\left\{\mathrm{DFT}_{2N}\left\{G^*_{B\to A}\right\}\mathrm{DFT}_{2N}\left\{I_B{}^*\right\}\right\}\right], \tag{6.63}$$

$$Q_{A\to B} = \mathrm{TR}_N\left[\mathrm{DFT}_{2N}^{-1}\left\{\mathrm{DFT}_{2N}\left\{G^*_{A\to B}\right\}\mathrm{DFT}_{2N}\left\{I_A{}^*\right\}\right\}\right], \tag{6.64}$$

$$Q_{B\to B} = \mathrm{TR}_N\left[\mathrm{DFT}_{2N}^{-1}\left\{\mathrm{DFT}_{2N}\left\{G^*_{B\to B}\right\}\mathrm{DFT}_{2N}\left\{I_B{}^*\right\}\right\}\right], \tag{6.65}$$

and the asterisk * denotes the complex conjugate.

Chapter 7

Numerical results

In this chapter we present the solutions for some practical configurations, which we calculated with the algorithms described in this report. First we tested the two-wire code for a few practical cases, which were verified with an independent MoM solution (Numerical Electromagnetics Code; NEC [8]). Second, a few results are presented for a three-dimensional inhomogeneous dielectric sphere in the presence of a thin-wire antenna.

7.1 Coupling between two wires

In this section we present the results of some two-wire configurations. First we test the algorithm with two wires with infinite conductivity, so that these results can be verified with NEC. After verification, some other interesting configurations will be examined for wires with infinite conductivity. Second, we examine the influence of finite conductivity of the wires on currents inside the wires. The results are presented in such a way that, if appropriate, the left plot represents the current on wire A and the right plot represents the current on wire B.

7.1.1 Wires with infinite conductivity

In this section we start of with two wires of equal length. The first configuration we look at consists of two wires with lengths λ, radii 0.01λ and conductivities $\sigma = \infty$. The distance between the center points of the wires is $d = 0.5$ m. The frequency of operation is $f = 300$ MHz. This frequency will be used for every configuration throughout this report unless stated otherwise. The results are presented in Figure 7.1 A and 7.1 B. The vertical axis of the plots represents the currents on wire A or B, respectively. The horizontal-axis represents the position on the wire divided by λ. As can be seen, the WCG-FFT method matches the results of NEC. However, the δ-gap driven wire (wire A) seems to show some deviation at certain points. This is due to the fact that the excitation of the wire is spread over the domain of integration by the weakening process.

The second configuration we look at, consists of two wires with different length. Wire A is in this case a shorter wire then wire B. We use this configuration to test if the convolution between the different Green's functions and the currents of wire A and B are evaluated

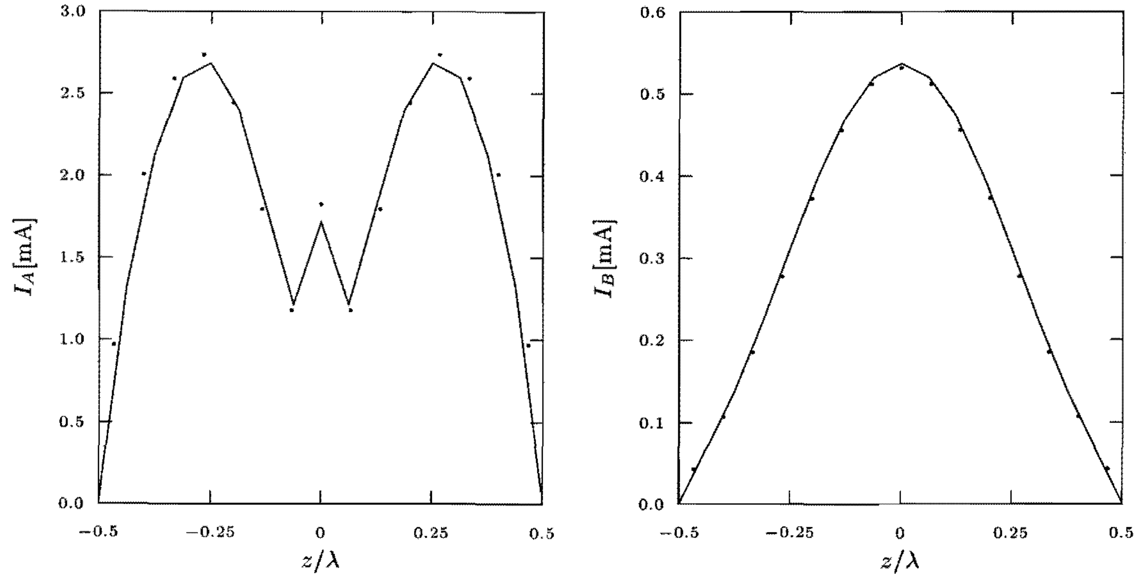

(A) (B)

Figure 7.1: *The induced currents on wires A and B with lengths* $L_A = L_B = \lambda$, *radii* $a = 0.01\lambda$, *conductivity* $\sigma = \infty$ *and distance* $d = \lambda/2$. *The solid lines represent results of the WCG-FFT method and the dots represent results of NEC.*

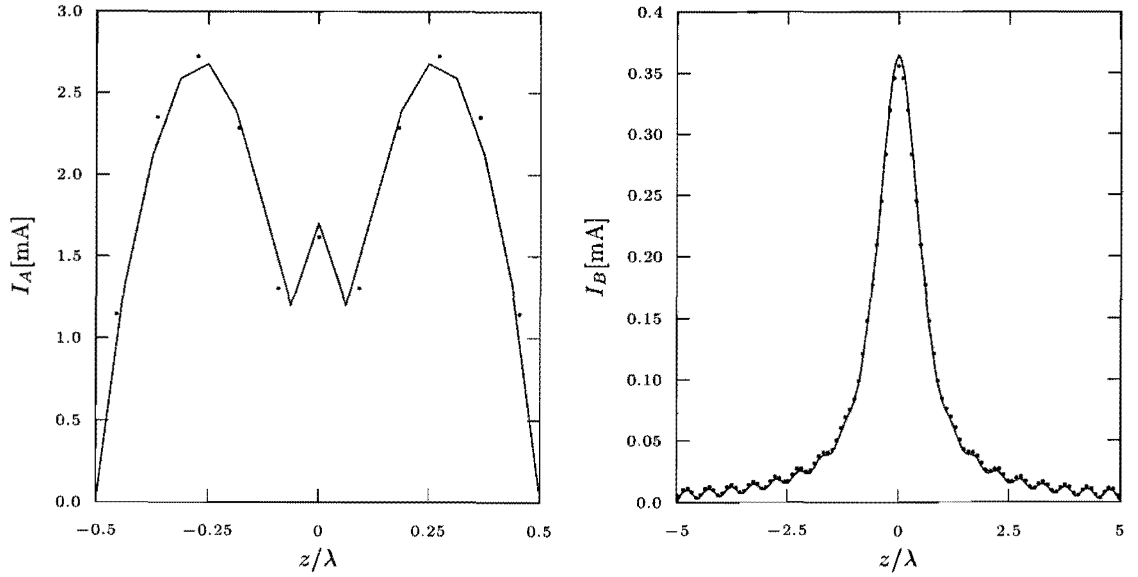

(A) (B)

Figure 7.2: *The induced currents on wires A and B with lengths* $L_A = 1$ *m*, $L_B = 10\lambda$, *radii* $a = 0.01\lambda$, *conductivity* $\sigma = \infty$ *and distance* $d = \lambda/2$. *The solid lines represent results of the WCG-FFT method and the dots represent results of NEC.*

correctly. In this particular configuration, the lengths of the wires are $L_A = \lambda$ and $L_B = 10\lambda$. The radii are again $a = 0.01\lambda$, distance $d = \lambda/2$ and $\sigma = \infty$. The results are plotted in

Figure 7.2. Again the results of the WCG-FFT method are a good match to the NEC results. Note that the results presented here apply for perfectly conducting wires ($\sigma = \infty$). A final test to show that our method is accurate is to plot the impedance of two configurations. The results have been achieved for a very large distance $d \approx \infty$ between wire A and wire B so that the influence of wire B on wire A is negligible. Wire A in the first configuration has a length of $L_A = 0.06$ m. The resonant frequency f_{res} will be $3e8/(2 \cdot 0.06) = 2.5$ GHz. Wire A in the second configuration has a length of $L_A = 1.59$ m and the resonant frequency f_{res} will be 94 MHz here. The results are plotted in Figure 7.3 and Figure 7.4, where the real

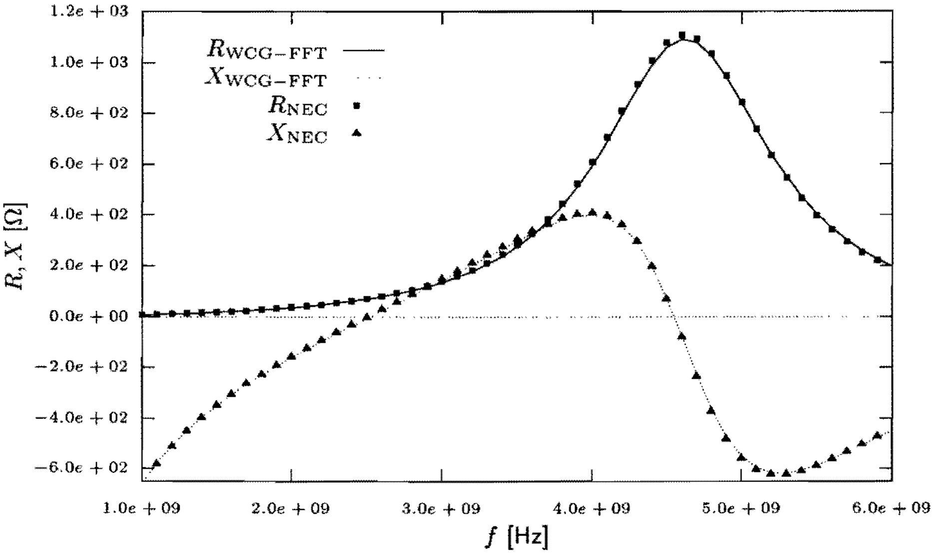

Figure 7.3: *Impedance plot of a wire with length* $L = 0.06$ *m. The solid and dashed line represents WCG-FFT and the boxes and triangles represent NEC.*

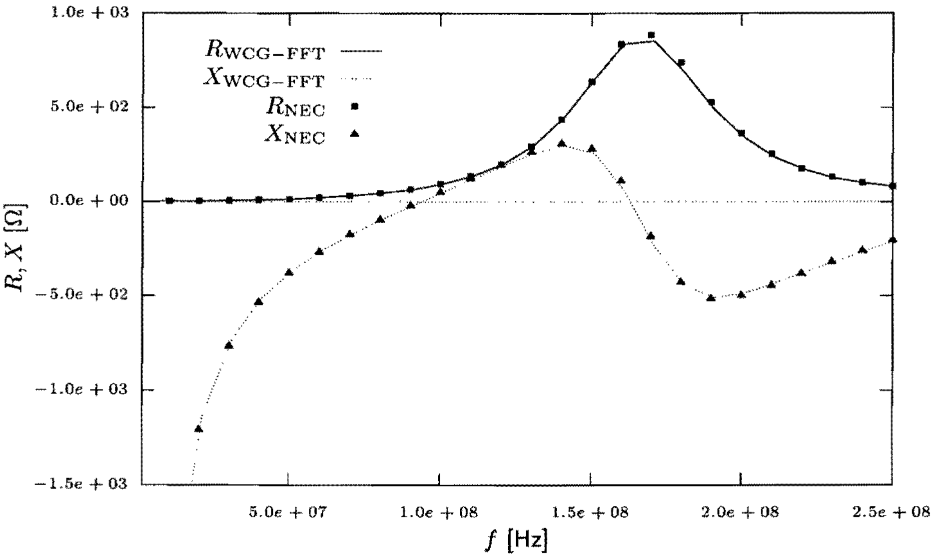

Figure 7.4: *Impedance plot of a wire with length* $L = 1.59$ *m. The solid and dashed line represents WCG-FFT and the boxes and triangles represent NEC.*

part (R) and imaginary part (X) of the impedance are plotted separately. As can be seen the results match the NEC-results. Also the resonant frequencies (the point where the reactance of the wire equals zero) is exactly at the point where it is expected. Now that the WCG-FFT has been shown to properly represent the current behavior on the wires and that also the impedance plots are accurate, we can start to examine some other interesting configurations. In Figures 7.5 and 7.6 we are looking at the influence of the distance d on the currents on wire A and B. The first configuration, without referring to NEC, we are looking at (see Figure 7.5) is again for infinite conductivity. The lengths of both wires are λ, the radii $a = 0.01\lambda$. The distance between the wires are $d = \lambda/2$, $d = \lambda/5$ and $d = 3\lambda/20$ respectively. Except for the change in the current distribution around the excitation point, only a minor change is observed in the current distribution on wire A due to the closer proximity of wire B. The shape and magnitude of the current induced on wire B however is strongly dependent on the distance between the wires. When the distance between the wires decreases, the magnitude of the induced current on wire B increases and the passive wire generally takes over the shape of the current on wire A. The wires A and B thus start to behave like the conductors in a two-wire transmissionline (TEM mode) if the distance between the wires is small. To see if this effect also takes place on the wires of different lengths, we again look at the configuration where the lengths of the wires are $L_A = \lambda$ and $L_B = 10\lambda$, radii $a = 0.01\lambda$ and the distance is again $d = \lambda/2$, $d = \lambda/5$ and $d = 3\lambda/20$, respectively. The results are plotted in Figure 7.6. We again observe a negligible change in the magnitude and shape of the current on wire A. The effect on wire B however, is much bigger than with the λ wire of the previous configuration. The shape of the current on wire B starts to resemble the form of wire A if the distance is

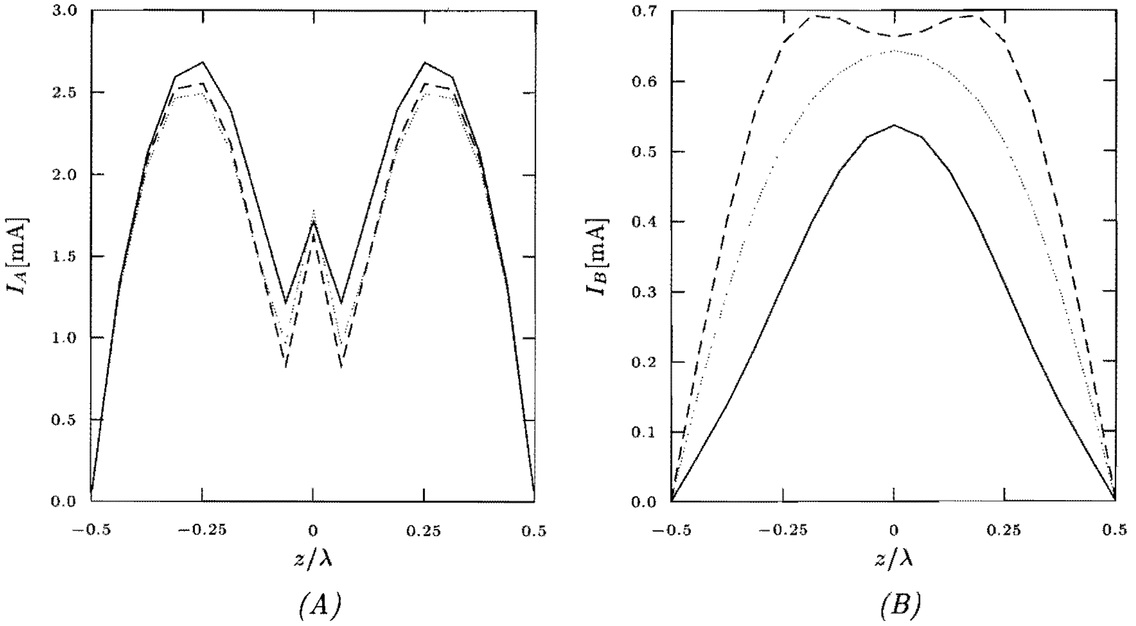

Figure 7.5: *Induced currents on wires with lengths* $L_A = L_B = \lambda$, *radii* $a = 0.01\lambda$, *conductivities* $\sigma = \infty$ *and distances* $d = \lambda/2$ *(solid line)*, $d = \lambda/5$ *(dotted line) and* $d = 3\lambda/20$ *(dashed line).*

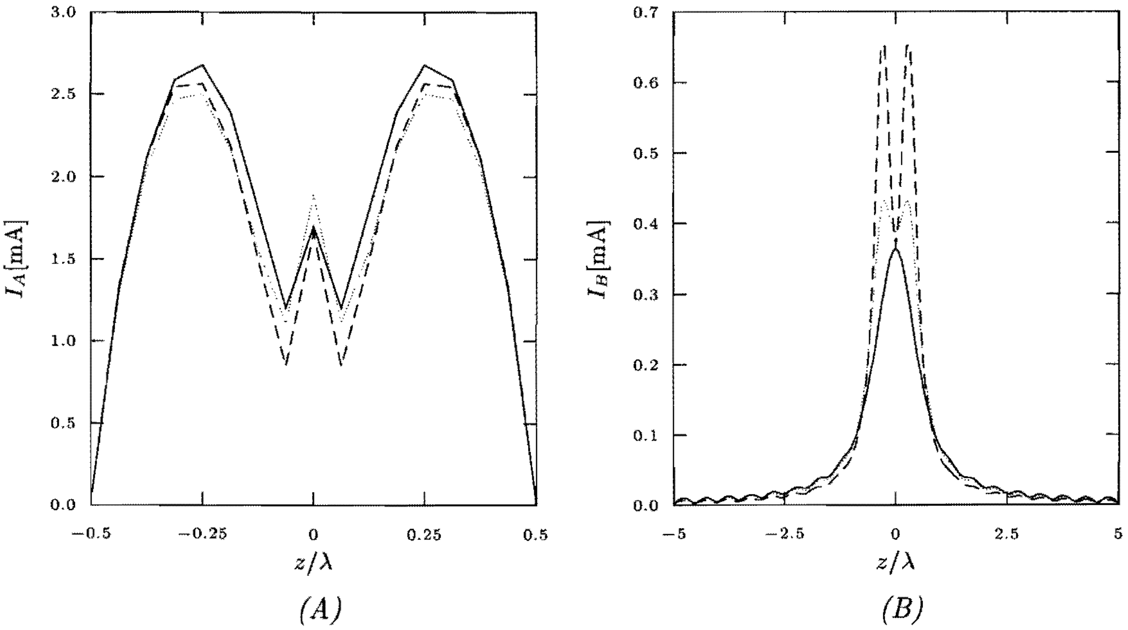

Figure 7.6: *Induced currents on wires with lengths* $L_A = \lambda$, $L_B = 10\lambda$, *radii* $a = 0.01\lambda$, *conductivities* $\sigma = \infty$ *and distances* $d = \lambda/2$ *(solid line),* $d = \lambda/5$ *(dotted line) and* $d = 3\lambda/20$ *(dashed line).*

only $d = \lambda/5$. We also see that the magnitude of the currents in the part of wire B where wire A is directly across wire B increases while in the other parts of wire B the magnitude decreases. We conclude that decreasing the distance between the wires results in an increase of the magnitude of the current on the passive wire (we have not yet used finite conductivity). Besides the increase in magnitude, the shape of the current distribution on the wire is affected. This effect seems to be bigger in the configuration with a large wire. The explanation for the bigger effect on the large wire can be explained by the fact that the endeffects with the larger wire are almost vanished compared to the short wire. In other words, the large wire can follow the shape of the current on wire A more easy.

7.1.2 Wires with finite conductivity

In the next configurations, we will examine the influence of different conductivities on the magnitude as well as on the shape of the current in the wires. We look at two wires of equal length ($L_A = L_B = \lambda$). Both wires have a radius of $a = 0.01\lambda$ and the distance between the wires is $d = \lambda/2$. The results for three different conductivities are plotted in Figure 7.7. The current for a larger conductivity has been omitted here since it is almost identical to the distribution for the largest conductivity considered here. This can be expected from Figure 4.3 and the formula for the factor which it represents (Eq. (4.47)). The magnitude of the current on both wires decreases with decreasing conductivity. The change in magnitude becomes more dramatic when the conductivity reaches a value of $\sigma = 50$ S/m. Since this is not a realistic value for metallic conductors, we may neglect the decrease in magnitude of the

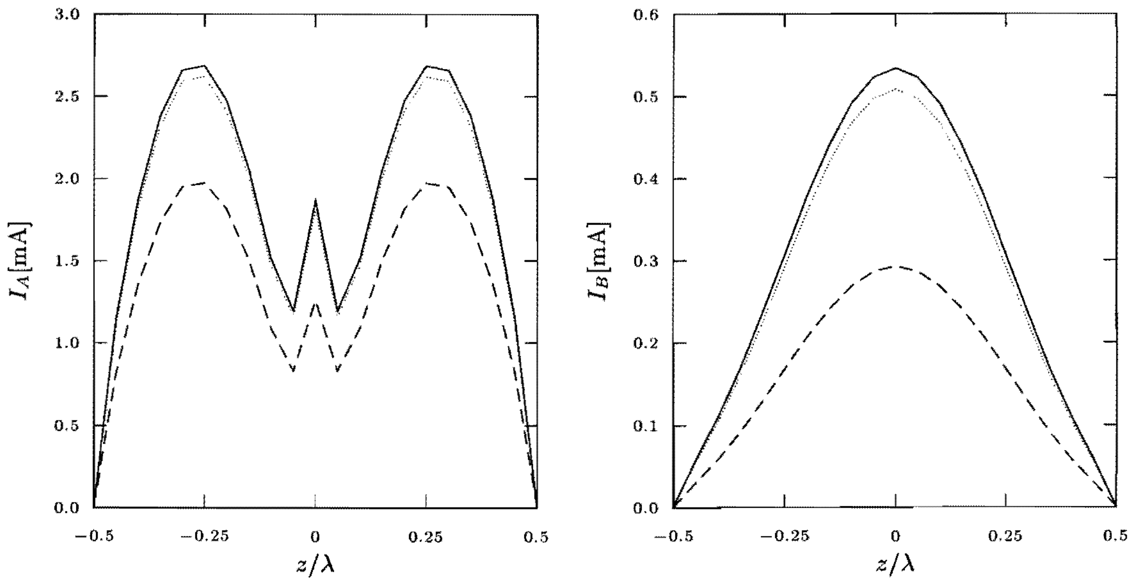

(A) *(B)*

Figure 7.7: *induced currents on wires with lengths* $L_A = L_B = \lambda$, *radii* $a = 0.01\lambda$ *and distance* $d = \lambda/2$. *The conductivity of the wires is* $\sigma = 5e5$ *S/m (solid lines),* $\sigma = 5e3$ *S/m (dotted lines) and* $\sigma = 5e1$ *S/m (dashed lines).*

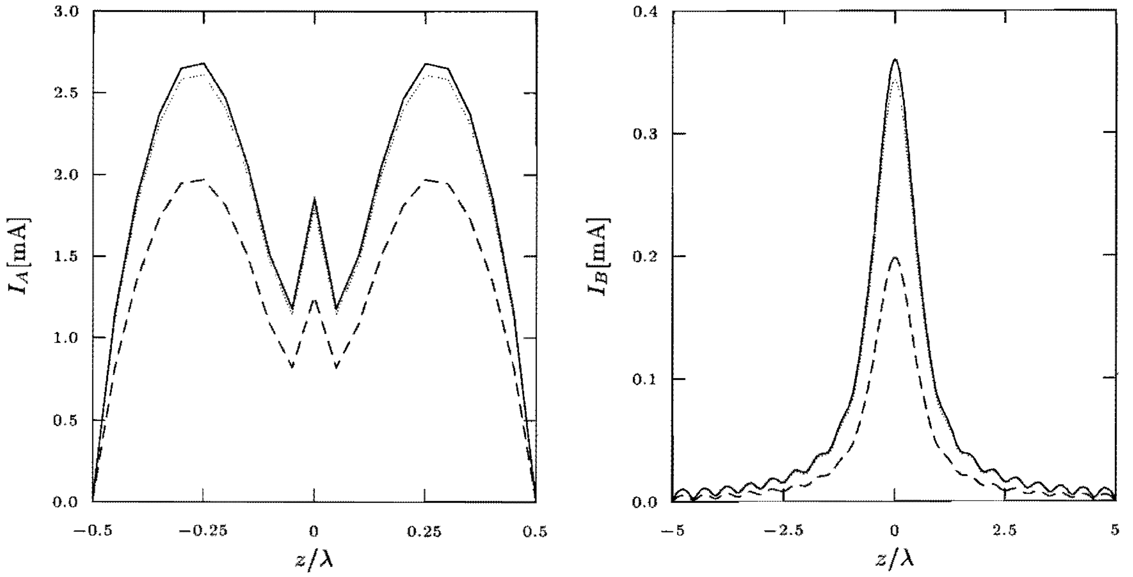

(A) *(B)*

Figure 7.8: *induced currents on wires with lengths* $L_A = \lambda$ *and* $L_b = 10\lambda$, *radii* $a = 0.01\lambda$ *and distance* $d = \lambda/2$. *The conductivity of the wires is* $\sigma = 5e5$ *S/m (solid lines),* $\sigma = 5e3$ *S/m (dotted lines) and* $\sigma = 5e1$ *S/m (dashed lines).*

current for practical applications. The shape of the current on both wires is not affected by the different conductivities. The same observations can be made if we look at a configuration where the lengths of the wires are $L_A = \lambda$ and $L_B = 10\lambda$. Both wires have again a radius of $a = 0.01\lambda$ and the distance between the wires is $d = \lambda/2$. From these results we may conclude that a realistic conductivity ($\sigma = 1e7, ..., 1e8$ S/m) does not affect the shape and the magnitude of the current at a fixed frequency if the length of the wire is not much smaller than the wavelength. Note that this effect is very much influenced by the relation between wavelength and the length and radius of the wire.

The last configuration we look at is the same as the previous configuration (see Figure 7.8), except for the distance, which is chosen $d = \lambda/4$ here. The results are plotted in Figure 7.9. Again the observation that the shape and magnitude of the current in the wire is not much affected for realistic values of the conductivity can be made. Thus, we can conclude that a realistic conductivity has little effect on both magnitude and shape of the current in a wire.

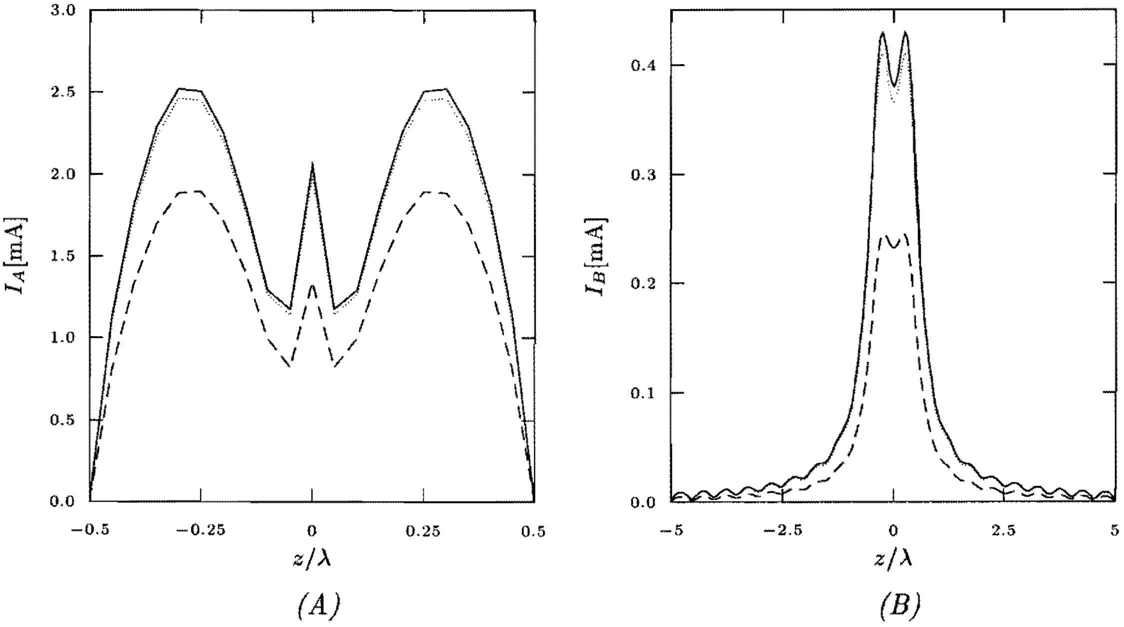

(A) (B)

Figure 7.9: *induced currents on wires with lengths* $L_A = \lambda$ *and* $L_B = 10\lambda$*, radii* $a = 0.01\lambda$ *and distance* $d = \lambda/4$*. The conductivity of the wires is* $\sigma = 5e5$ *S/m (solid lines),* $\sigma = 5e3$ *S/m (dotted lines) and* $\sigma = 5e1$ *S/m (dashed lines).*

7.2 Coupling between a wire antenna and a biological body

In this section we present the results of the influence that the radiated field of a wire antenna has on a biological body. A value we are particularly interested in is the specific-absorption rate (SAR) as stated earlier. The SAR is defined as

$$\mathrm{SAR} = \frac{\sigma|\mathbf{E}|^2}{2}, \tag{7.1}$$

which is defined in W/Kg.

7.2.1 Description of the configuration

The configuration we look at consists of a layered sphere as depicted in the left part of Figure 7.10 and a $\lambda/2$ dipole (see also Figure 5.2). The layered sphere consists of muscle ($\epsilon_r = 72$, $\sigma = 0.9$ S/m) and fat ($\epsilon_r = 7.5, ; \sigma = 0.05$ S/m). The radius of the inner sphere is 0.075 m and of the outer sphere is 0.15 m. The distance between the center of the sphere and the feed-point of the dipole (see Figure 7.10) is denoted as d. The length of the dipole is $\lambda/2$. The frequency of operation is 915 MHz.

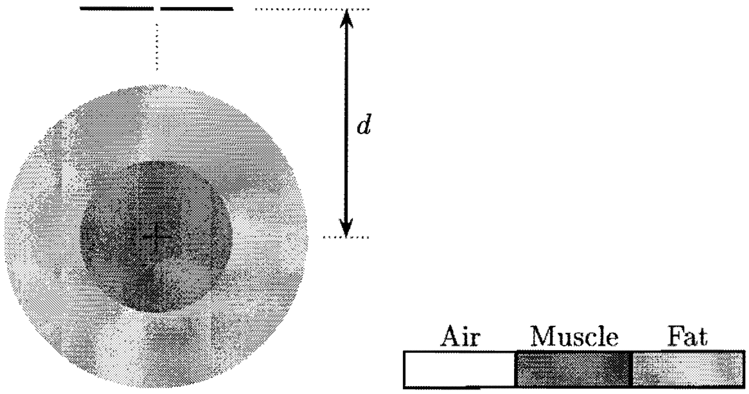

Figure 7.10: *Position of the dipole with respect to the cross section of the three-dimensional body*

7.2.2 Proximity effects on the SAR

In this section we look at the effect of decreasing the distance d on the SAR. First we look at the SAR distribution if the body is illuminated with a plane wave, where the front of the plane wave is parallel to the dipole in Figure 7.10. This distribution is compared to the SAR distribution where the distance between dipole and the center of the biological body is $d = 0.9$ m ($\approx 3\lambda$). As can be observed from Figure 7.11 there is a difference in the dynamic range of the absorbed power inside the sphere between the dipole (Figure 7.11B) and plane wave configuration (Figure 7.11A). For dipole excitation (Figure 7.11B) most of the power is absorbed in the fat region, while for plane-wave excitation (Figure 7.11A) we also find a part of the maximum absorbed power in the muscle region. In addition to the difference in dynamic range of the SAR, we can see that the power distribution inside the sphere also gives a horseshoe-like shape if we look at the maximum values of the SAR.

Next we look at the effect of the distance d on the SAR distribution inside the layered sphere. The results for various distances are depicted in Figure 7.12. Note that the SAR values in the different configurations are relative to the maximum SAR in case the distance $d = 0.17$ m. We observe that the SAR distribution still has the horseshoe-like shape as the distance is reduced to $d = 0.5$ m (Figure 7.12B). A change in the shape is observed as the distance is

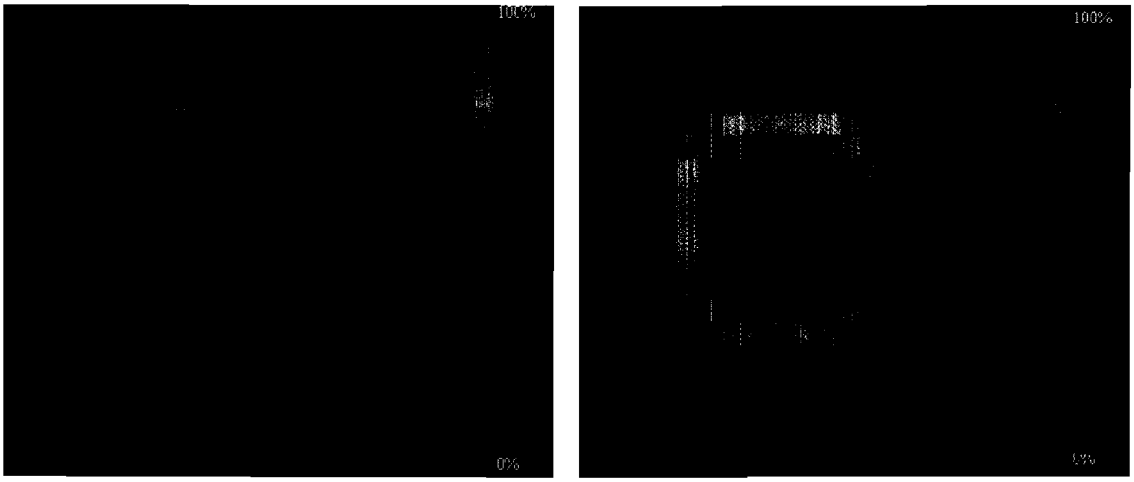

(A) (B)

Figure 7.11: *Comparison of the SAR distribution in a layered sphere due to plane wave illumination (A) and dipole interaction (B)*

decreased to $d = 0.2$ m (Figure 7.12C). The pattern now has two lobes which contain the maximum SAR. This pattern does not change much as we decrease the distance once more to a value of $d = 0.17$m. The lobe pattern can be explained if we look at the radiation pattern of the electric field of a dipole. Most of the electric field is radiated at the tips of the dipole. So this is in fact the same effect as we saw in the two-wire configurations, the radiation pattern of the electric field of the dipole has a strong effect on the SAR distribution inside the sphere if the distance is reduced.

If we look at all the configurations from Figure 7.12, it is again observed that the dynamic range of the SAR distribution is not as big as in the plane wave configuration (Figure 7.11A).

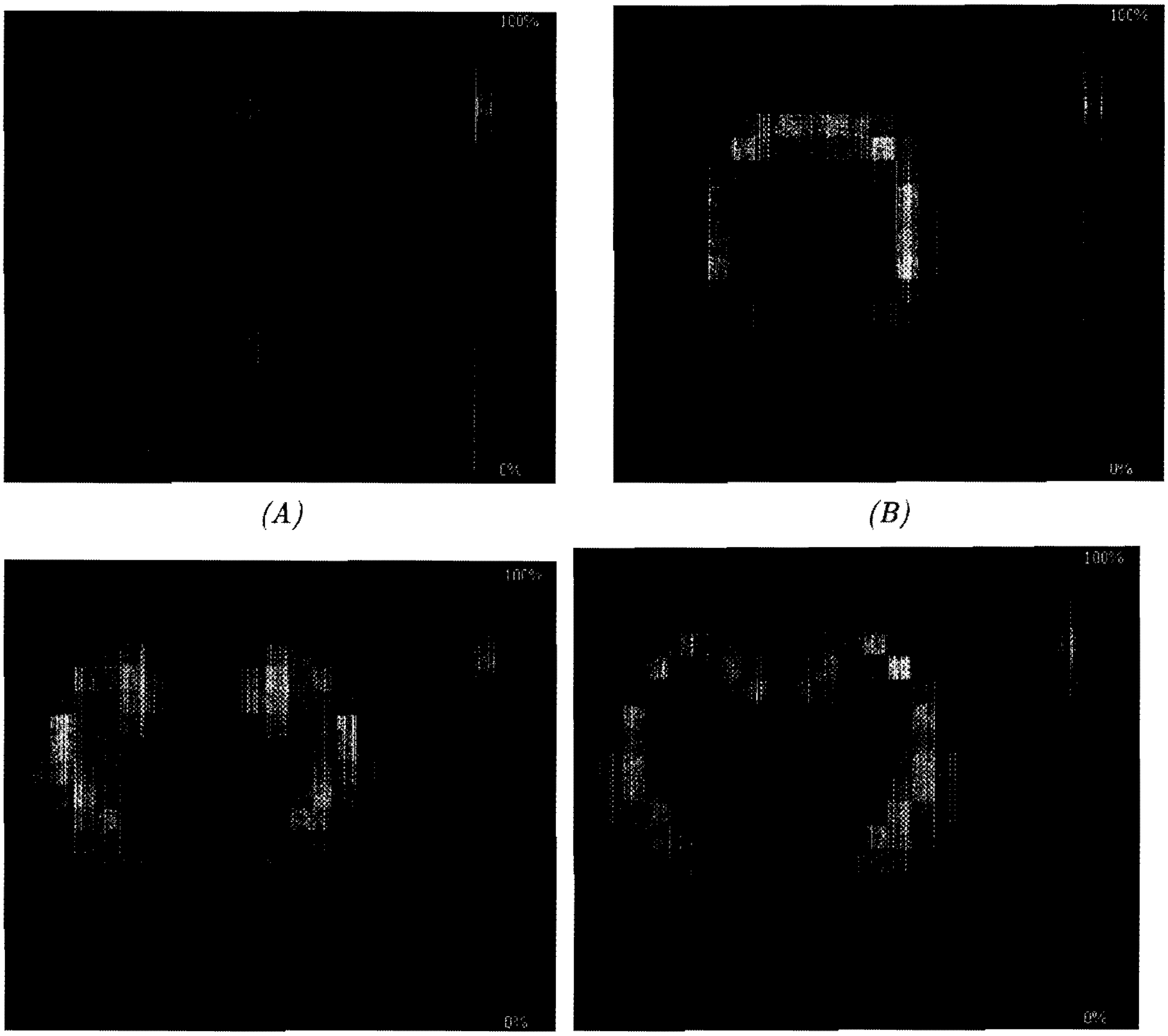

(A) (B)

(C) (D)

Figure 7.12: *Different SAR distributions due to dipole interaction at distances d=0.9 m (A), d=0.5 m (B), d=0.2 m (C) and d=0.17 m (D). The intensity is defined 100% at the maximum SAR in case the distance d=0.17 m and 0% in case of zero*

Chapter 8

Conclusions and recommendations

In this report we derived a general form of two coupled integral equations that describe the electromagnetic coupling between two three-dimensional bodies. This method has tested first for the special case of two wire antennas. The current on the wires with perfect conductivity proved to be accurate compared to NEC. It has been observed that the current distribution in a wire with finite conductivity (when σ assumes a realistic value for metallic conductors) did not deviate much from the distribution in a perfectly-conducting wire. The current started to deviate for very low values of the conductivity (at least for metallic conductors). The configurations where we looked at the influence of distance d between a passive wire and a delta-gap driven wire showed some interesting results. If the distance between the wires was decreased, it has been observed that the current distribution inside the passive wire gradually takes over the shape of the current in the active wire. The effect on the active wire was a change in the current distribution around the excitation point. We also looked at proximity effects with two wires of different lengths. The same observations as in the equal length case have been made here. However the effect of the current taking over the shape of the current on the active wire seemes more dramatic on the passive wire in the different length case when the distance d was decreased. Altogether we proved that our integral equation is accurate. The effects of finite conductivity could only be observed here as a magnitude effect. However the conclusion that this does not affect the current in the wire much for realistic conductivities and high frequencies (300 MHz - 1 GHz) still holds. The effect on the delta-gap driven wire was negligible (except in de gap region).

Next we looked at the influence on the SAR of the distance d between a dipole and a biological body. For a larger distance (typically $d = 2\lambda$ to $d = 3\lambda$) it was observed that the shape of the SAR distribution in case the body interacts with a dipole is almost the same as in the case where the body is illuminated with a plane wave. The only difference in the SAR distribution is the dynamic range which is bigger in the plane-wave case. If the distance is decreased to less than λ, the shape of the SAR distribution adapts to the radiation pattern of the electric field of the dipole. That is, the maximum SAR is concentrated in two lobes which are located under the tips of the dipole. We proved that our integral equation for the full three-dimensional problem is also accurate. We looked at the effect of the electric field radiated by the dipole on the biological body only qualitatively.

Finally we would like to make some recommendations for future research. Our model now describes the mutual coupling between a wire antenna and a dielectric object. This model has to be adapted to handle more complex structures which resemble, for instance, the human head more accurately. If we want some accurate values of the SAR at certain points in the biological body, we have to calculate how much input power should be given to the antenna. To connect a temperature rise to the specific-absorption rate (SAR), the model should also contain blood flow and convection flow inside the arteries. The effects of nose, ears, etc. (with the appropriate dielectric parameters) on the SAR could also be investigated.

Bibliography

[1] P.M. van den Berg, A.T. de Hoop, A. Segal and N. Praagman, "A computational model of electromagnetic heating of biological tissue with application to hyperthermic cancer therapy," *IEEE Trans. Biomedical Eng.*, Vol. BME-30 (1983), No. 12, pp. 797-805.

[2] P.M. van den. Berg, "Iterative computational techniques in scattering based upon the integrated square criterion," *IEEE Trans. Antennas Propagat.*, Vol. AP-32 (1984), No. 10, pp. 1063-1071.

[3] P.M. van den Berg, "Iterative schemes based on the minimazation of error in field problems," *Elektromagnetics* (1985), No. 5, pp. 237-262.

[4] J. van. Bladel, "Some remarks on Green's dyadic for infinite space," *IRE Trans. Antennas Propagat.*, Vol. AP-9 (1961), pp. 563-566.

[5] J. Boersma, Lecture Notes "Functietheorie," Eindhoven, The Netherlands: Eindhoven University of Technology, No 2383, Course 1994/1995.

[6] D.T. Borup and O.P. Gandhi, "Fast Fourier transform method for calculation of SAR distributions in finely discretized inhomogenous models of biological bodies," *IEEE Trans. Microwave Theory Tech.*, Vol. MTT-32 (1984), No. 4, pp. 355-360.

[7] E.O. Brigham, "*The Fast Fourier Transform*," New Jersey: Prentice Hall, 1974.

[8] G.J. Burke and A.J. Poggio, "Numerical electromagnetics code (NEC-2), methods of moments; Part III: User's guide," Lawrence Livermore Laboratory, California, Report UCID 18834, 1981.

[9] M.F. Cátedra, R.P. Torres, J. Basterrechea and E. Gago, "*The CG-FFT Method*," London: Artech House, 1995.

[10] K.M. Chen, "Interactions of electromagnetic fields with biological bodies," In: *"Research Topics in Electromagnetic Wave Theory,"* J.A. Kong (Ed.), New York: John Wiley & Sons, 1981.

[11] K.M. Chen and B.S. Guru, "Internal field and absorbed power density in human torsos induced by 1-500 MHz EM waves," *IEEE Trans. Microwave Theory Tech.*, Vol. MTT-25 (1977), No. 9, pp. 746-756.

[12] B.S. Guru and K.M. Chen, "Experimental and theoretical studies on electromagnetic fields induced inside finite biological bodies," *IEEE Trans. Microwave Theory Tech.*, Vol. MTT-24 (1976), No. 7, pp. 433-440.

[13] M.J. Hagman, O.P. Gandhi and C.C. Durney, "Numerical calculation of electromagnetic energy deposition for a realistic model of man," *IEEE Trans. Microwave Theory Tech.*, Vol. MTT-27 (1979), No. 9, pp. 804-809.

[14] M.K. Hessary and K.M. Chen, "EM local heating with HF electric fields," *IEEE Trans. Microwave Theory Tech.*, Vol. MTT-32 (1984), No. 6, pp. 569-576.

[15] M.F. Iskander, "Computational techniques in bioelectromagnetics," *Computer Physics Communications*, Vol. 68 (1991), pp. 224-254.

[16] C.C. Johnson, C.H. Durney and H. Massoudi, "Long-wavelength electromagnetic power absorption in prolate spheroidal models of man and animals," *IEEE Trans. Microwave Theory Tech.*, Vol. MTT-23 (1975), No. 9, pp. 739-747.

[17] K. Karimullah, "*Theoretical and Experimental Study of The Proximity Effects of Thin-Wire Antenna in Presence of Biological Bodies*," Michigan: Michigan State University, 1979. Doctoral Dissertation. Ann. Arbor Mich.: University Microfilms.

[18] K. Karimullah, K.M. Chen and D.P. Nyquist, "Electromagnetic coupling between a thin-wire antenna and a neighbouring biological body: Theory and experiment," *IEEE Trans. Microwave Theory Tech.*, Vol. MTT-28 (1980), No. 11, pp. 1218-1225.

[19] F.T.C. Koenis, "*The computation of the RCS of chaff using the weak form of the conjugate gradient FFT method*," TNO-FEL, The Hague, the Netherlands, Report FEL-93-A241, 1993.

[20] K.S. Kunz and R.J. Luebbers, "*The Finite Difference Time Domain Method for Electromagnetics*," Boca Raton: CRC Press, 1993, pp. 11-49.

[21] D.E. Livesay and K.M. Chen, "Electromagnetic fields induced inside arbitrarily shaped biological bodies," *IEEE Trans. Microwave Theory Tech.*, Vol. MTT-22 (1974), No. 12, pp. 1273-1280.

[22] D.P. Nyquist, K.M. Chen and B.S. Guru, "Coupling between small thin-wire antennas and a biological body," *IEEE Trans. Antennas Propagat.*, Vol. AP-25 (1977), No. 6, pp. 863-866.

[23] K.D. Paulsen, X. Jia and J.M. Sullivan jr., "Finite-element computations of specific absorption rates in anatomically conforming full-body models for hyperthermia treatment analysis," *IEEE Trans. Biomedical Eng.*, Vol. BME-40 (1993), No. 9, pp. 933-945.

[24] K.C. Pocklington, "Electrical oscillations in wires," *Cambridge Philosophical Society*, Vol. 9 (1897), pp. 324-332.

[25] A. Rubio Bretones and A.G. Tijhuis, "Transient excitation of a wire antenna in front of an interface," In: "*IEEE Antennas and Propagation Society International Symposium 1994. 1994 International Symposium Digest Antennas and Propagation,*" Seattle, june 20-24 1994, New York: IEEE, 1994, Vol. 3, pp. 2250-2253.

[26] A. Rubio Bretones and A.G. Tijhuis, "Transient excitation of two coupled wires over an interface between two dielectric half spaces," *Radio Science*, Vol. 32 (1997), No. 1, pp. 25-41

[27] R.J. Spiegel, "The thermal response of a human in the near zone of a resonant thin-wire antenna," *IEEE Trans. Microwave Theory Tech.*, Vol. MTT-30 (1982), No. 2, pp. 177-185.

[28] J.A. Stratton, "*Electromagnetic Theory,*" New York: McGraw-Hill Book Company, Inc., 1941, pp. 524-537.

[29] A. Taflove, "*Computational Elektrodynamics: The Finite Difference Time Domain Method,*" London: Artech House, 1995, pp. 51-92 and 145-202.

[30] C.T Tai, "*Dyadic Green's Functions in Electromagnetic Theory,*" New York: International textbook Company, 1971.

[31] A.G. Tijhuis, Z.Q. Peng and A. Rubio Bretones, "Transient excitation of a straight thin-wire segment: A new look at an old problem," *IEEE Trans. Antennas and Propagatation*, Vol. AP-40 (1992), No. 10, pp. 1132-1146.

[32] A.G. Tijhuis, Lecture notes "Computational techniques for transient scattering," Eindhoven, The Netherlands: Eindhoven University of Technology, available from the Electromagnetics section, Course 1994/1995.

[33] S.H.J.A. Vossen, A.G. Tijhuis and A.P.M. Zwamborn, "Mutual coupling between two wires of different length and finite conductivity," In: "*IEEE Antennas and Propagation Society International Symposium 1997. 1997 International Symposium Digest Antennas and Propagation,*" Montreal, july 13-18 1997, Canada: IEEE, 1997, Vol. 2, pp. 784-787.

[34] A.P.M. Zwamborn, "*Scattering by Objects With Electric Contrast,*" Delft: Delft University of Technology, 1991, Doctoral Dissertation. Delft: Delft University Press.

[35] A.P.M. Zwamborn and P.M. van den Berg, "The three-dimensional weak form of the conjugate gradient FFT method for solving scattering problems," *IEEE Trans. Microwave Theory Tech.*, Vol. MTT-40 (1992), No. 9, pp. 1757-1766.

[36] A.P.M. Zwamborn and P.M. van den Berg, "Computation of electromagnetic fields inside strongly inhomogenous objects by the weak-conjugate-gradient fast-Fourier-transform method," *J. Opt. Soc. Amer. A*, Vol. 11 (1994), No. 4, pp. 1414-1421.